UNIVERSITY OF CRETE

DEPARTMENT OF PHYSICS

Degree Thesis

The dependence of X-ray variability of AGN on black hole mass and accretion rate

Student: Vasilis Binas Valavanis

Supervisor: Prof. Iossif Papadakis

Contents

CHAPTER 1: INTRODUCTION

1.1 Active Galactic Nuclei

As the title suggests, in this project, we will work with X-ray data of Active Galactic Nuclei, thus let us introduce some of their basic properties and a brief historical overview. Generally, AGN (Active Galactic Nucleus) refers to the existence of energetic phenomena in central regions of galaxies which cannot be attributed to stars.

Approximately 10% of galaxies in the near universe host active nuclei. AGN are divided in many subclasses. The main division is between "radio loud" and "radio quiet", which are bright and faint in radio wavelengths, respectively. Among radio quiet AGN, originally the two largest groups were Seyfert and quasars, with their main difference being the amount of radiation emitted by the compact central source. On one hand, in the average Seyfert galaxy, the nuclear source emits an amount of total energy at visible wavelengths comparable to the energy emitted by all of the stars in the galaxy. On the other hand, in the typical quasar, the nuclear source is around 100 times or more brighter than the stars. Historically, the appearance of quasars did not initially suggest identification with galaxies, which made their correlation to Seyferts poor.

1.2 Seyfert galaxies

We will focus on Seyfert Galaxies, since radio loud (or "beamed") AGN may have their emission dominated by synchrotron emission from particles which move with relativistic velocities in very well collimated outflows that are called "jets". Seyfert galaxies were first detected in 1908 by Edward A. Fath and Vesto Slipher, who used the Lick Observatory and thought they were observing "spiral nebulae". The first to realize that there are several similar galaxies which form a distinct class was Carl Seyfert (1943). Seyfert studied the spectra of galaxies that had high central surface brightness, i.e. stellar like cores, and found that the optical spectra are dominated by high-excitation nuclear emission lines. Figure 1 shows the optical spectrum of a Seyfert 1 galaxy (NGC 5548). The noticeable characteristics of the spectrum are:

- The optical/UV emission rises sharply at small wavelengths/high frequencies, this spectral component is called the "Big Blue Bump", contrary to what is observed in normal galaxies, where the emission at UV wavelengths usually decreases with increasing frequency.

- The presence of very broad emission lines. It is believed that their width is due to Doppler broadening. In this case, the large width implies that the line emitting gas clouds should move with velocities up to $\sim 8000 - 10000 km/s$.

We can now estimate, roughly, the mass of the nucleus in AGN. As we already mentioned, the line emitting gas may move with high velocity. If we assume Keplerian orbits around the nucleus of mass M, then

$$M = u^2 R/G,$$

where R is the distance between the gas clouds and the nucleus, while the cloud velocity, u, can be obtained from the widths of the emission lines. The line flux is variable and correlated with the continuum variations but with a delay of the order of $\sim 3 - 10 days$, thus we can estimate the distance $R \approx ct \approx 0.004 pc$ for $t = 5 days$. Therefore, the mass of the nucleus is $M \sim 1.6 \cdot 10^7 M_\odot$ for $u = 4000 km/s$.

Seyfert galaxies are classified in many subclasses depending on the presence of emission lines of different width in their optical spectra. The sample of galaxies we will study includes Seyferts of Type 1, 1.9 and 2. The first type refers to Seyferts galaxies which show both broad and narrow lines in their optical spectra. On the other hand, Seyfert 2 galaxies show only narrow lines in their spectra. The last type, Seyfert 1.9, refers to galaxies where the broad component is detected only in the $H\alpha$ line and not in the higher-order Balmer lines.
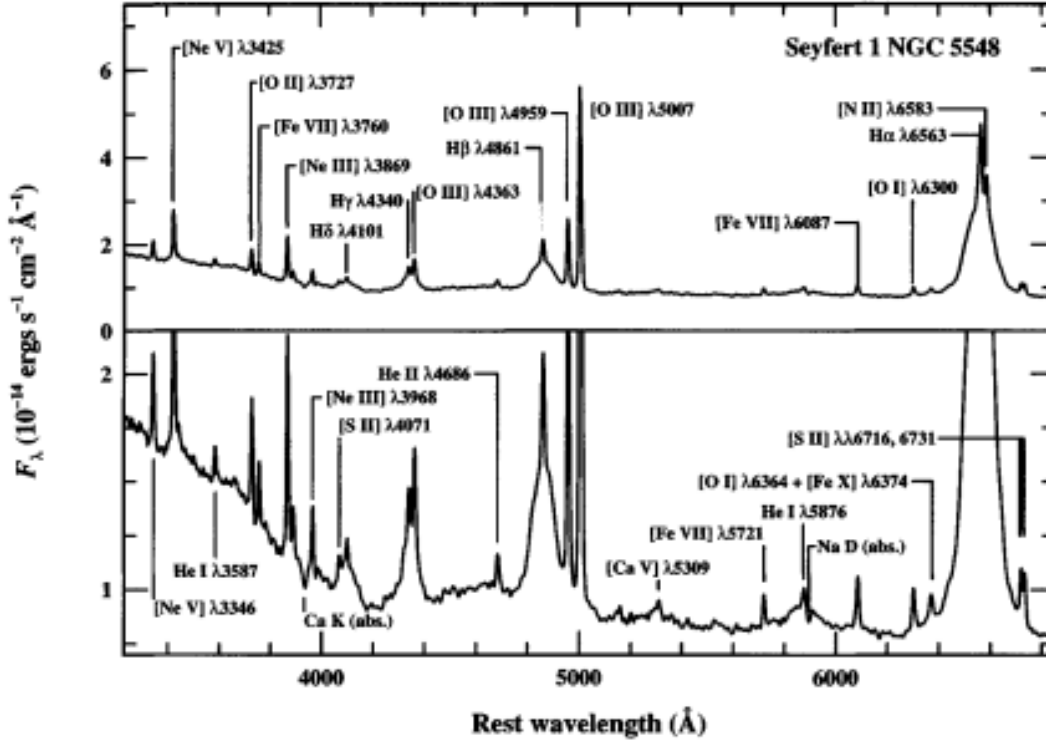
Figure 1: The optical spectrum of the Seyfert 1 galaxy NGC 5548. The prominent broad and narrow emission lines are labeled, as are strong absorption features of the host galaxy spectrum. The vertical scale is expanded in the lower panel to show the weaker features. The full width at half maximum (FWHM) of the broad components is about 5900 $km\ s^{-1}$, and the width of the narrow components is about 400 $km\ s^{-1}$. (Figure taken from B.M.Peterson, An Introduction to Active Galactic Nuclei, 1997).

1.3 Unification theory

The unification theory proposes that the physical processes that operate in AGN are the same in all objects, irrespective of their type. Those types are different because we observe them from a different angle. For example, Seyfert 1s are radio quiet AGN we view from an angle where we can directly see the nucleus (see Fig. 2). That is the reason we observe both broad and narrow lines from gas clouds with high velocities that are close to the nucleus and gas clouds with lower velocities that are further away from the nucleus, respectively. On the other hand, Seyfert 2s are observed from a viewing angle where the putative dusty torus, surrounding the accretion disk, obscures the broad line emissions (Fig. 2).

1.4 Current paradigm

It is currently believed that AGN are powered by accretion of matter in the form of a disk (called the "accretion disk") to a supermassive black hole ($10^6 - 10^{10} M_\odot$) at the center of galaxies. As matter falls into the black hole (BH) it releases gravitational energy, which eventually heats the disk. For supermassive BHs, the luminosity that the disk emits peaks in the optical-ultraviolet waveband, and this explains the observed Big Blue Bump.

Also, AGN are strong X-ray emitters. Figure 3 shows the plot of luminosity ($v \cdot F_v$) versus frequency for a large sample of quasars. The lines indicate the mean spectral energy distribution of AGN, when divided in three luminosity bins. Red, black and blue lines show the mean spectrum of the low, medium and high luminosity AGN, respectively. We can identify the Big Blue Bump around $\sim 4000 - 1000$Å. The lines below ~ 60Å indicate the mean spectrum of AGN in the X-ray band. This emission cannot originate

4

from the accretion disk, as the disk's temperature cannot be high enough for it to emit X-rays. Recent studies have found that $\sim$ 10% of the overall luminosity emitted by an AGN is in the X-ray area. We currently believe that X-rays in AGN are produced by inverse Compton scattering of disk photons by hot electrons with large energies ($\sim 100 - 200 \, keV$) located in a region which is called as "X-ray corona".
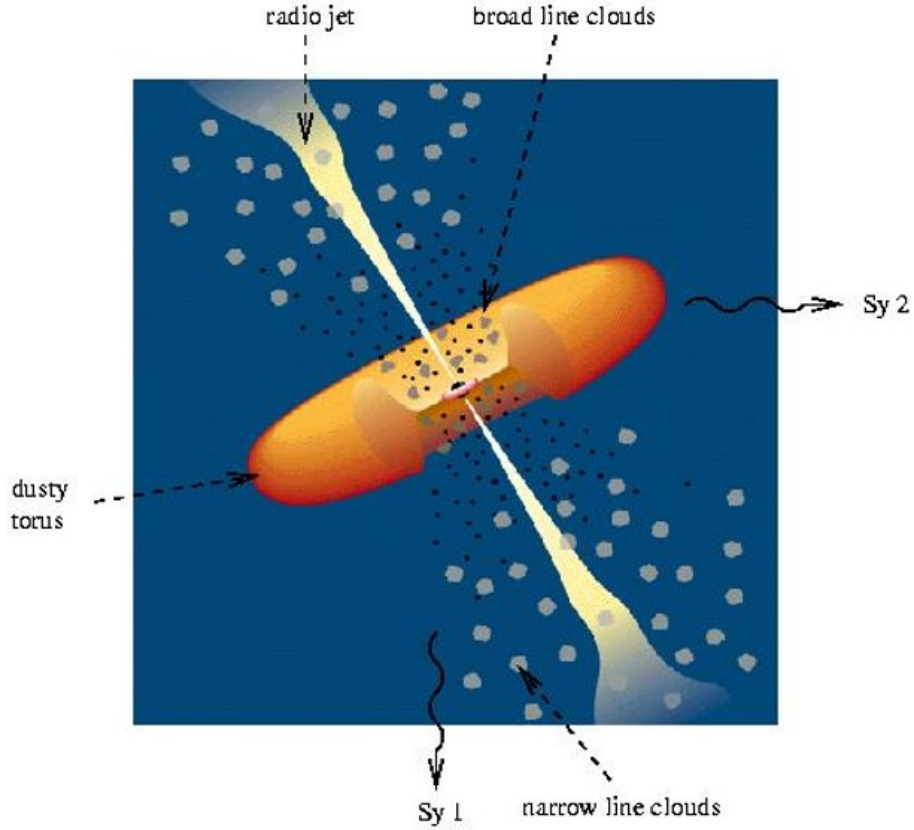

Figure 2: The AGN structure as proposed by unification theory, figure taken from https://wwwmpa.mpa-garching.mpg.de/HIGHLIGHT/2003/highlight0301_diagram.png.
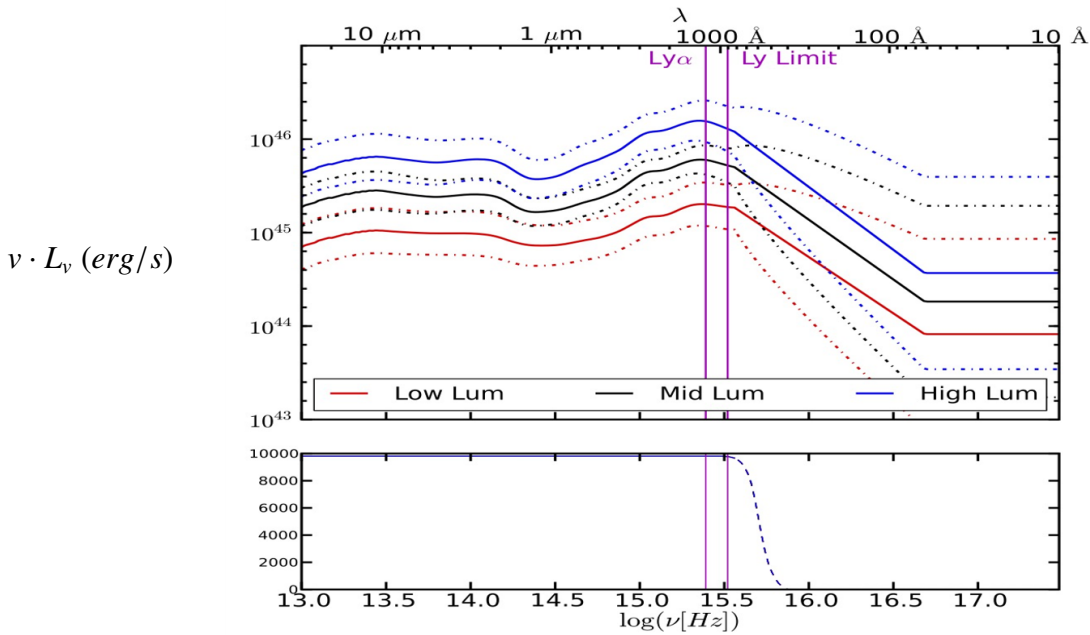

Figure 3: Plot of luminosity (erg/s) vs frequency (or wavelength, in the x-axis) for a large sample of AGN. Figure taken from Krawczyk C. et al (2013).

1.5 AGN variability

In general, AGN are highly variable at all wavelengths. In fact, variability is a defining characteristic of AGN. Figure 4 shows a plot of flux versus time of an AGN named NGC 4151 in different spectrum bands. X-axis has a time span of around 2 months. It is clear that this AGN is highly variable at all wavelengths. The top plot (light blue) shows the X-ray light curve. Figure 4 shows that the amplitude and time scales are larger and shorter, respectively, in the X-ray band. The variations in the other light curves are smoother and of lower amplitude. Since X-rays are emitted from a region which is thought to be close to the BH, the study of X-ray emission (i.e. the X-ray energy spectrum and its variations) is important, as it can give information about the physical processes around the BH.
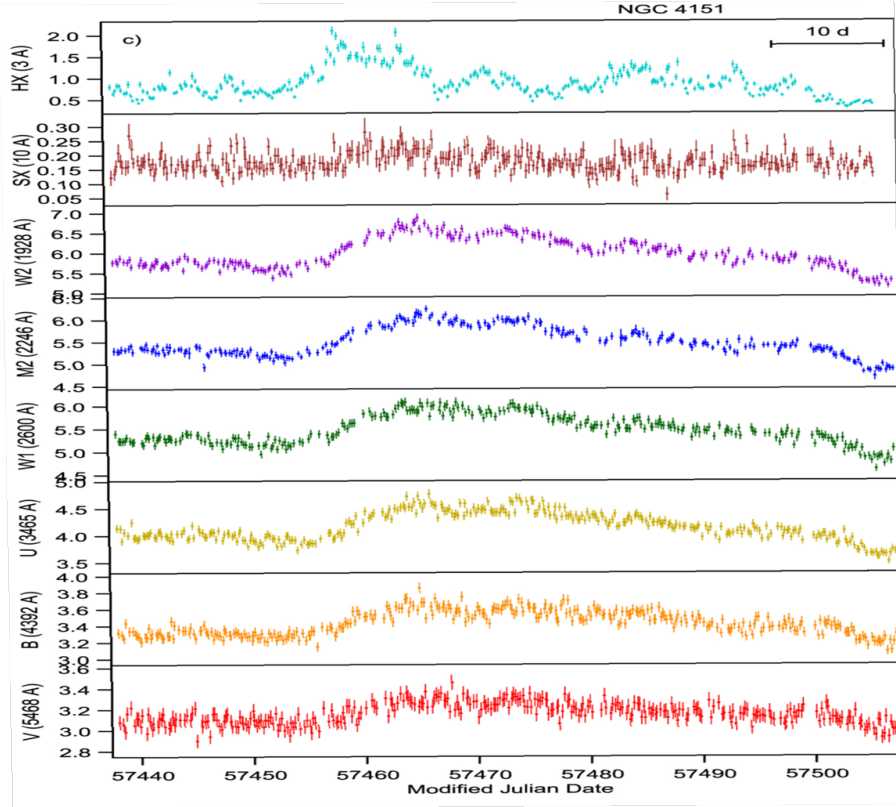

Figure 4: Plot of flux vs time of NGC 4151 in different spectrum bands. Figure taken from Edelson R. et al. (2019).

1.6 Objective of this work

The main aim of this work is to study the X-ray variability of AGN using $14 - 195 \, keV$ high quality light curves obtained from observations with the instrument BAT on board of the X-ray satellite *Swift* . The BAT has observed many AGN and has produced continuous, evenly sampled, and long light curves. This gives us the opportunity to study the variability from time scales of a month up to 13 years. Thus analysing the BAT light curves is ideal to study the X-ray variability. Using the BAT light curves we can compute the power spectrum in order to investigate whether and how the power spectrum density (i.e the variability mechanism) depends on black hole mass and/or accretion rate. In addition, the fact that the BAT detects the AGN emission at energies higher than $\sim 15 - 20 \, keV$, implies that the light curves show intrinsic variations both for Type 1 and Type 2 objects, since these X-rays should not be absorbed even in most Type 2 objects (where the gas density is very high).

6

CHAPTER 2: POWER SPECTRUM ESTIMATION

2.1 The sample

Koss et al. (2022) published a catalog of active galactic nuclei as part of the second data release of the *Swift* BAT AGN Spectroscopic Survey. Among the 1210 sources in the BAT 70-month survey, they have identified all AGN, 858, and have estimated black hole masses for most of them. Our sample consists of the 100 brightest AGN (in the $14 - 195\ keV$ band) of the Koss et al. (2022) sample. The only exception is Q0241+622, because it lacks an accretion rate estimate. In choosing the sources we excluded: a) "beamed" AGN (i.e. objects classified as "BZQ", "BZG" and "BZB"), since their emission may be dominated by the jet emission, and b) "dual" AGN (listed in Table 4 of Koss et al. (2022)), if the ratio of the predicted $F^{obs}_{14-195keV}$ of the fainter source over the total detected BAT flux was larger than 1%.

The sources in our sample are listed in the Appendix (Table 2). The source classification, redshift, logarithm of the BH mass, and logarithm of λ_{Edd}, where $\lambda_{Edd} = L_{Bol}/L_{Edd}$ (L_{Bol} and L_{Edd} are the bolometric and Eddington luminosity[1], respectively) are listed in columns 2, 4, 5 and 6, and are taken from Koss et al. (2022). According to these authors, L_{Bol} is calculated from the intrinsic luminosity in the $14 - 150\ keV$ range, using a bolometric correction factor of 8. We assume that λ_{Edd} is a measure of $\dot{m}$, i.e. of the ratio of the accretion rate, $\dot{M}$, over the Eddington accretion rate, $\dot{M}_{Edd}$. Koss et al. (2022) classified the unbeamed AGN in three categories, namely: Sy1, Sy1.9 and Sy2, based on the presence of broad H_β lines, narrow H_β but broad H_α, or only narrow optical lines in their optical spectra, respectively. The second column of Table 2 lists the spectral classification of the sources. Finally, in the third column of Table 2 we list the mean observed flux in the 14-195 keV, $F^{obs}_{14-195keV}$, taken from the *Swift* BAT, 157-Month Hard X-ray Survey (https://swift.gsfc.nasa.gov/results/bs157mon/).

2.2 The light-curves

We retrieved the BAT light-curves for all the sources in the sample from the *Swift* -BAT 157 month survey web page. We considered the monthly, Crab-weighted light-curves in the $14 - 195\ keV$ band. Figure 5 shows the light curves of 4 sources in our sample. Cen A and NGC4151 (in the top panels) are the brightest Sy2 and Sy1 sources in the sample, respectively, while ESO490-26 and LEDA170194 (bottom left and right panels, respectively) are Sy1 and Sy2 AGN, with fluxes which are representative of the average/low flux levels in the sample. The count rate of the sources plotted on the upper panels is clearly variable. On the other hand, it is more difficult to understand if the sources plotted in the lower panels are variable as well. This difference in the variability behaviour could be due to the fact that the sources on the bottom panels are significantly fainter than the sources in the upper panels.

The 157 month light-curves are constructed with similar methods as those in the 105 month release (Oh et al. 2018), with some updates in both the instrumental calibration and responses. Figure 6 shows plots of the source count rate in the first 105 months of the *Swift* observations, as computed in the 105-month survey light-curves (Oh et al. 2018) versus the count rate in the 157 month survey light curves we use in this project, for four sources. The plots in Fig. 6 show that the 105 and 157 survey count rates are consistent with each other (within the errors), over the common time period.

A few points in some light curves (such as some points plotted in fig. 5) are associated with large error bars. We found that the exposure time of most of these points is less than 5 *ksec* (a small number when compared to the nominal bin width of 1 month). We use the mean of the error (squared) to compute the Poisson noise level in the power spectrum (see 2.4). We therefore decided to remove these points and to replace them using linear interpolation between the adjacent points in the light curves, since these large

---

[1]Eddington luminosity is the maximum luminosity an object (such as a star) can achieve without breaking the balance between the force of radiation acting outward and the gravitational force acting inward. For pure ionized hydrogen, $L_{edd} = \frac{4\pi GMm_p c}{\sigma_T}$, where σ_T is the Thomson scattering cross-section for the electron, m_p is the mass of a proton, c is the speed of light, M the mass the central object and G is the gravitational constant.
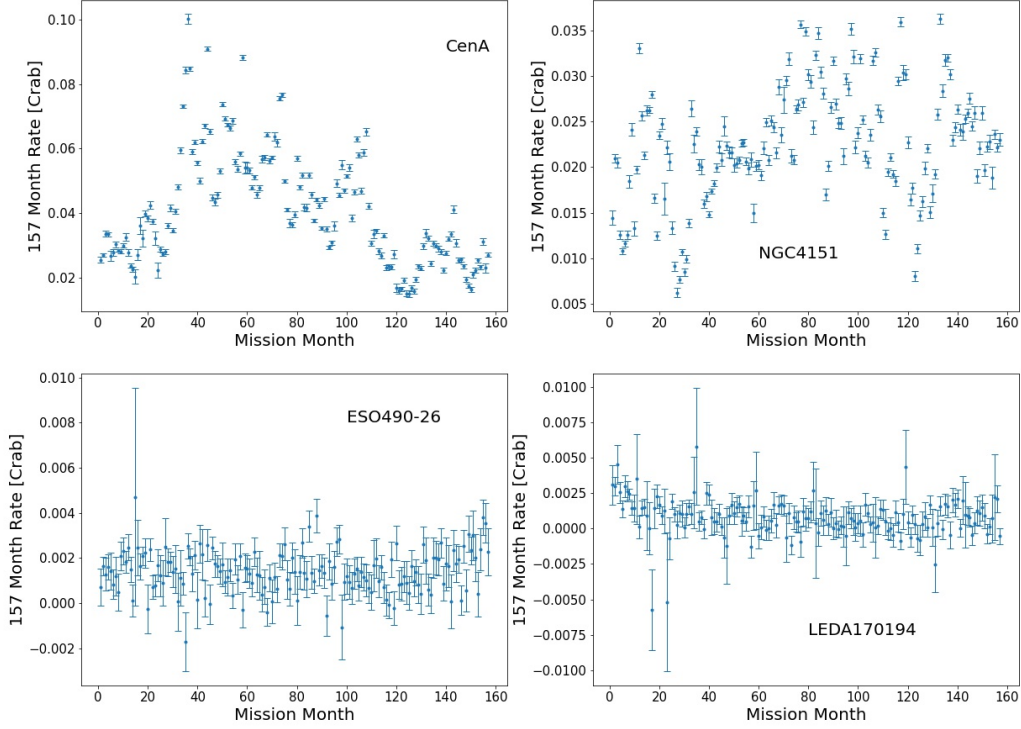
Figure 5: Plot of the monthly Crab-weighted light-curves as computed in the 157-month *Swift* survey for 4 sources: Cen A, NGC4151, ESO490-26 and LEDA170194.

errors can bias the mean squared error to a value that is not representative of the actual Poisson noise variance in the light curve.

Additionally, there are a few missing points in some light curves (*Swift* BAT, 157-Month Hard X-ray Survey), thus we filled them by using linear interpolation again. For each interpolated point we added a random error, assuming Gaussian statistics with a standard deviation equal to the mean error of all points in the light curves (excluding the ones with $\Delta t \leq 5\ ks$). There are 39 light curves with about two missing points and/or points with an exposure time less than $5\ ks$, on average.

2.3 The variable sources

We checked which sources show significant variations in the light curves using traditional χ^2 statistics. To this end, we computed the weighted mean of each light curve, and we fitted the light curves with a constant line, equal to the mean. The count rate error in the *Swift* -BAT light curves is inversely proportional to the square root of the exposure time in each bin (this is easily checked when plotting errors versus the respective exposure time), and it does not depend on the source's flux. In this case, the weighted rather than the straight mean is more representative of the source's mean flux. This process was done without considering the interpolated points. In order to determine if a source is variable or not, we computed the so-called χ^2 for each light curve as follows,

$$\chi^2 = \sum_{i=1}^{N} \frac{(x_i - \overline{x})^2}{\sigma_i^2},$$
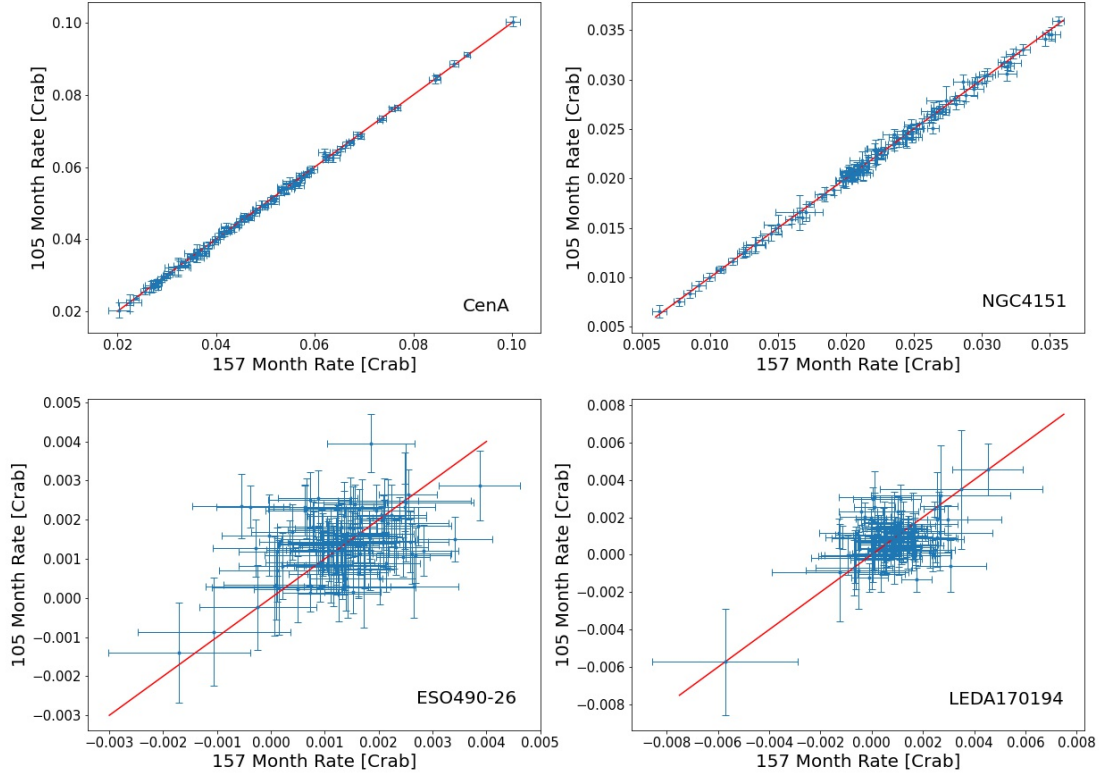
(1)

8

Figure 6: Plot of the count rate in the first 105 months of the *Swift* observations as computed in the 105-month survey light curves (Oh et al. 2018), versus the count rate in the 157-month survey light-curves that we use in this work, for four AGN in our sample. The red solid line in each plot shows the one-to-one relation.

where x_i is the count rate, $\bar{x}$ is the mean count rate of the source, σ_i is the error of x_i and N is the number of observations. Under the assumption that the errors on the light curve points are Gaussian then χ^2 is a random variable which is distributed according to a χ^2 distribution with N-1 degrees of freedom. If a source is highly variable, then we expect χ^2 to be much larger than the number of points in the light curve. In fact, we can compute the probability that χ^2 would have a certain value for a light curve, under the assumption that the light curve is not variable (P_{null}).

The resulting χ^2 values over the degrees of freedom (dof) are listed in the 7th column in Table 2 that was mentioned earlier. We accept that a light curve is variable if p_{null} is less than 0.01. Letters "V" or "NV" in the 8th column in Table 2 indicate whether a source is variable or not (i.e. $p_{null} < 0.01$ or $p_{null} \geq 0.01$, respectively). We found that 26 sources out of the 100 in our sample are non-variable. Nineteen of the NV sources are Sy1 and the rest are Sy2 and Sy 1.9. The mean $\log(M_{BH})$ and $\log(\lambda_{Edd})$ are ~ 7.8 and ~ -1.4, respectively, for both the V and NV group of sources. However, the ratio of the mean count rate over the mean error (i.e. the signal-to-noise ratio of the light curve) is smaller than 3 in almost all, but two, of the NV sources. On the contrary, the same ratio is larger than 3 in almost two thirds of the V sources. This result indicates that the main reason we do not detect significant variations in the NV sources is because their flux is low. Consequently, the amplitude of the variations due to the experimental noise is larger than the amplitude of the intrinsic variations and so we cannot detect them.

2.4 Power spectrum estimation

Power spectrum is a random function that is very useful when studying physical phenomena which are not deterministic, but random. The emission and detection of photons from a variable astronomical object is a random process. To study the variability of these objects, we usually measure the number of photons detected over a fixed period of time (say Δt). Such a record of photon numbers detected every Δt for a certain period of time is called the "light curve" of an astronomical object. The light curve cannot be described by a deterministic function of time, even for a source which is constant in flux over time. Instead, every count rate that has been measured belongs to a range of possible values and the relative "likeness" of these values is described by a probability distribution. If we observe again the same object, under the same conditions then, naturally, the record of the observed values would be different. This is due to the fundamental nature of the emission and detection process. In fact, each time we perform the experiment we will have different records. Each of these possible records is called a "realization" and the whole collection of them is called an "ensemble" of the process.

Let us consider a random process (i.e. the variable emission from an AGN), and let us assume that its statistical properties (such as the mean, variance, etc.) do not change over time (processes which have this property are called stationary). We cannot use the Fourier series or integrals to represent the variable signal, since they apply only to deterministic functions. We therefore have to consider every realization separately. However, each realization is not, in general, periodic and not all realizations decay to zero for time$\rightarrow \pm\infty$ (because by definition, the process is stationary). Here, Wiener's theory of "general harmonic analysis" can help in the representation of the process in the frequency space, by expressing each realization as a Fourier-Stielties transform, of the form,

$$X(t) = \int_{-\infty}^{+\infty} e^{it\omega} dZ(\omega), \tag{2}$$

where $dZ(\omega) = O(\sqrt{d\omega})$, meaning that the order of magnitude of the increment $Z(\omega)$ over an interval $d\omega$ is infinitesimal, but much larger than $d\omega$ (Priestley, 1981). The $dZ(\omega)$s in the equation above are complex numbers. Equation (2) defines the spectral representation $X(t)$, if it is a stationary, random process. Roughly speaking, $dZ(\omega)$ determines the amplitude of the sinusoids ($e^{i\omega t}$) into which we can decompose $X(t)$. In engineering, if $X(t)$ represents some physical process such as a current or voltage, the total energy dissipated by the process in any time interval is equal to the sum of the amounts of energy dissipated by each of the sine and cosine terms, which in fact, is proportional to the square of $dZ(\omega)$, i.e. $|dZ(\omega)|^2$. Therefore our main interest when studying variable phenomena lies in the squared amplitudes $|dZ(\omega)|^2$.

We can define the "density of energy per unit frequency" as follows,

$$q(\omega) = |dZ(\omega)|^2/d\omega,$$

which we expect to be a reasonably well behaved function of ω, since $|dZ(\omega)|^2$ should be of the order of $d\omega$ if $dZ(\omega) = O(\sqrt{d\omega})$. So far we have considered each realization of the random process separately, but $dZ(\omega)$, and hence $q(\omega)$, will change from realization to realization. In order to construct a function which describes the properties of the whole process, we take the average value of $q(\omega)$ over all realizations, i.e.

$$h(\omega) = \overline{q(\omega)} = \overline{|dZ(\omega)|^2}/d\omega,$$

where the overbar denotes the average taken over all realizations of the process. The function $h(\omega)$ is called the "power spectrum density function" of the process (PSD or power-spectrum) and it plays a fundamental role in the analysis of time variable phenomena in Astronomy. First of all, although $h(\omega)$ has a direct physical meaning in engineering, as a power density function, in many variable phenomena $h(\omega)$ has the important property that:

$$\sigma^2 = \int_0^\infty h(\omega) d\omega, \tag{3}$$

where σ^2 is the variance of the process. In other words, $h(\omega)d\omega$ is equal to the variance that each sinusoid of frequency ω contributes to the total variance of the process. As such, study of $h(\omega)$ as a function of frequency ω, can reveal characteristic time scales on which the variable process may operate. In addition, determination of $h(\omega)$ as a function of ω can help discriminate among various theoretical models for the variability mechanism of the observed variations, which should be able to predict $h(\omega)$.

2.4.1 Estimation of power spectrum in practise

Let us assume N observations, $x(t_i)$ of a variable AGN, at times $t_i, i = 1, 2, ..., N$, every Δt months. In practise it is customary to compute the so called periodogram,

$$I_N(f_j) = \frac{2\Delta t}{N} | \sum_{i=1}^{N} x(t_i)e^{-i2\pi f_j t_i} |^2 \quad (1/month^{-1}) \tag{4}$$

and consider it as an estimator of $h(\omega)$. The data in the equation above are normalized to the weighted mean (i.e. $x(t_i) = (x(t_i)-\overline{x})/\overline{x}$, with $\overline{x}$ being the light curve weighted[2] mean). The periodogram is calculated at the following set of frequencies:

$$f_j = j/(N\Delta t), j = 1, 2, ..., N/2. \tag{5}$$

In the case of the *Swift*/BAT light-curves, $N = 157$ and $j_{max} = 78$. The periodogram is an unbiased estimator of the intrinsic power spectrum and, if it is calculated only at the set of frequencies defined above, the periodogram estimates (i.e. $I_N(f_j)$) are independent variables. However, their error is not known, as it depends on the intrinsic $h(\omega)$ (which we wish to measure with $I_N(\omega)$).

2.5 Poisson noise error

Poisson noise, also known as photon noise, is a basic form of uncertainty associated with the measurement of light, which is attributed to the quantized nature of light and the independence of photon detections. When a sensor detects photons, each individual detection can be treated as an independent event that follows a random distribution. Thus, the count rate measurement, i.e. number of photons N detected over a time interval Δt, is a classical Poisson process and its discrete probability function is,

$$Pr(N = k) = \frac{e^{-\lambda\Delta t}(\lambda\Delta t)^k}{k!},$$

where λ is the expected number of photons per unit time interval, which is proportional to the incident flux. The equation above defines a standard Poisson distribution with $\lambda\Delta t$ being the rate parameter that corresponds to the expected incident photon count (i.e. to the mean value of the distribution). In the case of light curves, the term "poisson noise" refers to the variance of the Poisson process that is associated with the photon detection process and, due to the Poisson distribution properties, the variance is equal to the mean of the distribution, $\sigma_{PN}^2 = \lambda\Delta t (counts^2)$.

Based on what we discussed above, the count rate of an object we measure is equal to:

$$x_{obs}(t) = x_{int}(t) + \epsilon(t), \tag{6}$$

where $x_{int}(t)$ is the signal intrinsic to the source and $\epsilon(t)$ is a random variable representing the Poisson noise. If $\epsilon(t)$ is an uncorrelated process (i.e. $\epsilon(t')$ does not depend on $\epsilon(t)$, where $t \neq t'$) which does not depend on $x_{int}(t)$ either (as is the case with the BAT light curves we use) then one can show that,

$$h_{x,obs}(\omega) = h_{x,int}(\omega) + h_\epsilon(\omega), \tag{7}$$

---

[2]The weighted mean is computed as $\overline{x} = \frac{\sum x_i/\sigma_i^2}{\sum 1/\sigma_i^2}$, where x_i is the count rate and σ_i its error.

where $h_\epsilon(\omega)$ is the power spectrum of the Poisson noise process. If $\epsilon(t)$ has the properties we mentioned above, then $h_\epsilon(\omega)$ will have the same value at all frequencies, ω. Therefore, in order to estimate the intrinsic PSD, $h_{x,int}(\omega)$, we must first estimate $h_\epsilon(\omega)$, and then subtract the constant Poisson power spectrum (or Poisson noise level, C_P), from the periodogram. It can be shown that C_P can be computed as follows,

$$C_P = \frac{2\Delta t(\overline{\sigma_{err}^2})}{\overline{x}^2}, \tag{8}$$

where $\overline{\sigma_{err}^2}$ is the mean of the squared error of the points in the light curve, which we assume is a valid estimator of the light curve variance due to the Poisson noise. Since the correct estimation of C_P is important for the accurate determination of the PSD, we used the periodograms of the NV sources to test how well eq. (8) works in practice.

First, we wanted to check if the periodograms of the NV sources are flat, as expected. To test this, we computed the logarithm of the periodogram, and we grouped them into groups of size $M = 20$. The resulting PSD estimates are approximately Gaussian distributed, with known error (e.g Papadakis & Lawrence, 1993, PL93 herefater). We discovered that a constant line provides a good fit to all the grouped logarithmic periodograms. Thus we confirmed that the periodograms of these sources are indeed flat, implying the lack of intrinsic variations with amplitude larger than the Poisson noise variations of the NV sources. In this case, the mean of the periodogram estimates should be representative of the Poisson noise level in the light-curves. Instead of the mean periodogram, we actually computed the mean of the logarithmic periodogram estimates as follows,

$$\log(C_{P,obs}) = \frac{\sum_{j=1}^{n_f}(\log[I_N(f_j)] + 0.25068)}{n_f}, \tag{9}$$

where $n_f = 78$ (the number of frequencies where we compute the periodogram), and we adopt 0.25068 in eq. (9), following Vaughan (2005). The number $\log(C_{P,obs})$ should be representative of the logarithm of the observed Poisson level in each NV source. Here, the reason for calculating $\log(C_{P,obs})$ instead of $C_{P,obs}$ is because the error of the former is known, and is equal to $\sqrt{0.31/n_f}$ (PL93).

Figure 7 shows a plot of the logarithm of the ratio of the "measured" Poisson noise ($C_{P,obs}$), over the "expected" Poison noise (C_P) versus $\log(C_P)$ for the NV sources. The solid line in the same figure shows the mean $\log(C_{P,obs}/C_P)$, which is equal to 0.026 ± 0.012. From the figure we conclude that the data are broadly consistent with this line, and since the mean $\log(C_{P,obs}/C_P)$ is consistent with zero too (within $\sim 2.2\sigma$), we conclude that C_P, as defined by eq. (8), provides a good estimate of the Poisson noise in the light curves.

Even though the solid line in Fig. 7 fits the data quite well, strictly speaking, the best-fit χ^2 value of 58.5 for 25 dof indicates that the quality of the fit is poor (P value $<<$ 0.01). This is due to four sources, where $\log(C_{P,obs}/C_P)$ is $\sim 2 - 3\sigma$ away from the mean. Thankfully, the disagreement between C_P and $C_{P,obs}$ in these sources does not indicate a systematic trend in Fig. 7; C_P is less than $C_{P,obs}$ in two objects, while the opposite is the case for the other two AGN. The results lead us to the conclusion that C_P may not (always) provide an accurate measurement of the Poisson noise on an *individual* light curve basis, but it gives a good estimate of $C_{P,obs}$, *on average*. Finally, since our work is based on the study of the average PSD of many sources in various groups, we adopt C_P, as defined by eq. (8), as an estimate of the Poisson noise in the *Swift*/BAT light curves. We multiply C_P by $10^{0.026} = 1.06$, to account for the fact that C_P may (slightly) underestimate the Poisson noise level, as indicated by the fact that the mean $\log(C_{P,obs}/C_P)$ is equal to 0.026. None of our results are affected significantly if we do not consider this factor.
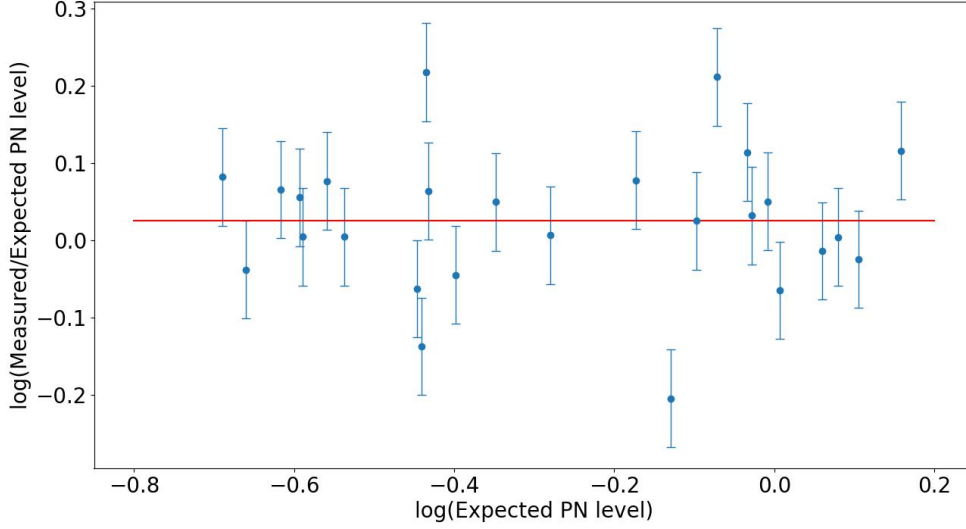
Figure 7: Plot of $\log(C_{P,obs}/C_P)$ versus C_P for the 26 NV sources in the sample. The solid line indicates the mean $\log(C_{P,obs}/C_P)$.

2.6 Computing and fitting the ensemble PSD of AGN

Even if the periodogram is an unbiased estimator of the intrinsic PSD, its statistical properties are not ideal for our work. The probability distribution of the periodogram estimates follows a χ^2 distribution with 2 degrees of freedom (which is very different than a Gaussian), while their variance is large and unknown. In fact, the variance does not even decrease with increasing data points. For that reason, it is customary to smooth the periodogram using various "spectral windows". However, smoothing in the linear space is not a good solution to our problem in the case of power-law like intrinsic PSD. One option would be to bin the logarithmic periodogram as suggested by PL93, but that is not efficient in our case. The periodogram of the *Swift*/BAT light curves is computed at 78 frequencies. If we would follow the prescription of binning the log periodogram into groups of size $M = 20$, we would end up with just four points in the power spectrum, over a limited frequency range. Fitting them with a straight line would result in best-fit parameters with large uncertainties (errors). To avoid this, we followed a different method to compute and find the best fits of the power spectra of the variable sources in our sample.

As we describe in the next section, we consider variable objects in relatively small groups in the $log(L_X)$ vs $log(M_{BH})$ plane (L_X will be defined in the next section). We compute the periodogram of each one of them, we subtract the Poisson noise level and then, at each of the ten lowest frequencies (i.e. up to $f = 10/157 \approx 0.064$ month^{-1}), we accept the mean of the periodograms of all sources in each bin,

$$P\hat{S}D(\nu_k) \equiv \overline{I(\nu_k)} = \frac{\sum_{i=1}^{n_{AGN}}[I_i(\nu_k) - C_{P,i}]}{n_{AGN}}, \qquad (10)$$

as an estimate of their ensemble, mean power spectrum at frequency ν_k, where $\nu_k = f_k, k = 1, 2, \ldots, 10$, and n_{AGN} is the number of AGN in each $[log(L_X), log(M_{BH})]$ group. At higher frequencies, the variance of the noise subtracted periodogram estimates increases. For that reason, we further smooth the mean PSD using a simple top-hat spectral window, as follows.

First we compute $\overline{I(f_j)}$ from eq. (10) at frequencies $f_j, j = 10, 11, \ldots, 75$ (we do not use the 3 final frequencies in our work), and then we accept the mean of 5 successive $\overline{I(f_j)}$'s, i.e.

$$P\hat{S}D(\nu_k) = \frac{\sum_{i=k+(k-11)*4}^{k+(k-10)*4} \overline{I(f_i)}}{5}, \qquad (11)$$

13

as an estimate of the mean power spectrum at frequencies,

$$\nu_k = \frac{\sum_{i=k+(k-11)*4}^{k+(k-10)*4} f_i}{5},$$ (12)

where $k = 11, 12, \ldots, 23$. This was possible, because the number of mean periodogram estimates that we bin at high frequencies is small, meaning that the smoothing process should not affect significantly the intrinsic PSD shape.

The number of AGN that we consider in each $[log(L_X), log(M_{BH})]$ group is small (see below), thus the probability distribution of the resulting PSD estimates, $P\hat{S}D(\nu_k)$, is not Gaussian, even at high frequencies. Therefore we cannot use traditional χ^2 statistics to fit the observed power spectra. For that reason, we assumed that the intrinsic PSD follows a power-law like shape. So we computed the logarithm of $P\hat{S}D(\nu)$, and we fitted a straight line to the $\log[P\hat{S}D(\nu_k)]$ vs $\log(\nu_k)$ data, of the following form,

$$\log(\text{PSD})(\nu) = \log(PSD_{amp}) + PSD_{slope} \cdot \log(\frac{\nu}{\nu_0}).$$ (13)

Here PSD_{amp} is the PSD amplitude at $\nu = \nu_0$, with $\nu_0 = 10^{-2}(\text{month}^{-1})$. The frequency 10^{-2} month^{-1} is close to the mean of the sampled frequencies and the error on the best-fit line amplitude is minimized when it is defined at that frequency. Lastly, we fitted the data following the ordinary least square (OLS), $[Y|X]$ prescription of Isobe et al (1990). In this way, even though we do not know the error of $\log[P\hat{S}D(\nu_k)]$, we can compute both the best-fit line parameters and their errors.

CHAPTER 3: POWER SPECTRUM ANALYSIS RESULTS

3.1 The Aliasing Effect

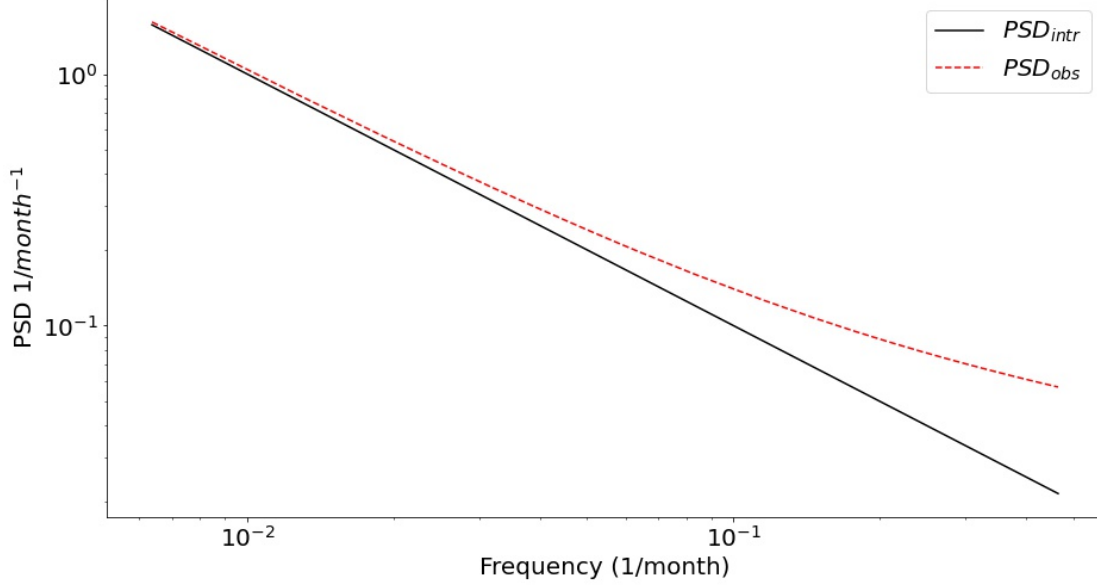**Figure 8:** $PSD_{intr/obs}$ vs frequency.

We work with count rate samples measured at time intervals $\Delta t = 1\,month$. However, light emission from AGN is continuous so it is clear that we miss information on high frequencies, thus our ability to estimate the high frequency end of the spectrum is negatively affected. Consider a spectral representation of the form presented in eq. (2). If we sample a continuous process at certain time intervals, Δt, then this representation extends only over the frequency range $(-1/2\Delta t, 1/2\Delta t)$. The main reason for this statements is that when time (t) is restricted to integers multiple of Δt, there is no distinction between the frequency components $e^{i\omega t}$ and $e^{i(\omega \pm 2k\pi/\Delta t)t}$, where $k = 1, 2, 3, ...$. All these components with frequencies $\omega \pm 2\pi/\Delta t, \omega \pm 4\pi/\Delta t, ...$ will appear to have identical frequency ω. They are said to be the "aliases" of ω and every component outside the range $(-1/2\Delta t, 1/2\Delta t)$ has an "alias" inside this range. In this case,

$$PSD_{obs}(f_j) = \sum_{k=0}^{\infty} PSD_{intr}(f_j + \frac{k}{\Delta t}), where \ k = 0, 1, 2.... \tag{14}$$

In order to determine whether aliasing may be a serious problem in our case we performed the following experiment. We consider an intrinsic PSD of the form:

$$PSD_{intr}(f) = (\frac{f}{0.01})^{-1}. \tag{15}$$

This is a power-law like power spectrum which has an amplitude of 1 at $f_0 = 0.01(month^{-1})$. We chose this PSD form, as it is similar to the observed PSDs of a few AGN at energies $2 - 10 \ keV$ (Markowitz et al, 2003). We also assume that this PSD "breaks" to a steeper slope (of -2), above a break frequency, $f_b = \frac{1}{T_b}$, where the break time scale, T_b, depends on the BH mass as

$$log(T_b) = 1.09log(M_{BH}) - 1.7, \tag{16}$$

where T_b is in units of days and M_{BH} is the BH mass in units of $10^6 M_\odot$ (Gonzalez Martin & Vaughan, 2011). For a BH of mass $10^{7.5}$ (similar to the median BH mass for the sources in our sample), $T_b = 0.86 days = 0.029 months$, and therefore $f_b = 34.8 (month^{-1})$. Solid black line in Fig. 8 shows the intrinsic PSD as computed from eq. (15), while red dashed line shows the observed PSD as computed from eq. (14), when $\Delta t = 1 month$ and $k = 0, 1, 2, ..., f_b \cdot \Delta t$, so that the maximum frequency which is aliased back to the $(\frac{1}{157\Delta t}, \frac{1}{2\Delta t})$ range is then one just below the break frequency. Figure 8 shows considering flattening for the observed PSD at frequencies higher $\sim 10^{-1} (month^{-1})$, in the case when we consider aliasing.

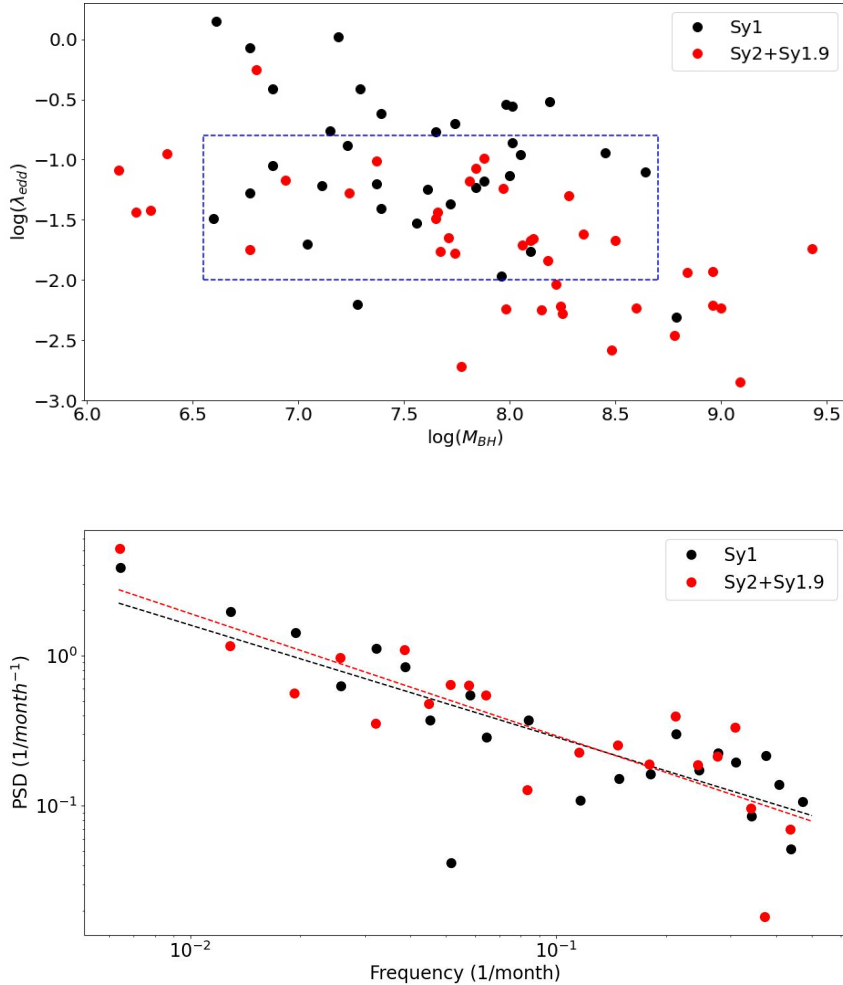## 3.2 Comparison between Type 1 and Type 2 AGN

Figure 9: *Upper panel:* Shows a plot of $\log(\lambda_{\text{Edd}})$ versus $\log(M_{\text{BH}})$ for the variable sources in the sample. Black and red circles indicate data for the Sy1 and Sy2 galaxies, respectively. The mean BH mass and accretion rate of the Sy1 and Sy2 sources in the dashed box are the same (within errors). *Lower panel:* Black and red points show the ensemble PSD of the Sy1 and Sy2 galaxies which are in the dashed box drawn in the upper panel. Black and red dashed lines show the best-fit line to the PSDs.

Firstly, we want to investigate whether the Sy1 and Sy2 power spectra are similar, or not. The top panel in Fig. 9 shows a plot of $\log(\lambda_{\text{Edd}})$ versus $\log(M_{\text{BH}})$ for all the variable sources in the sample. Black and red circles indicate the Sy1 and the Sy2 sources, respectively (hereafter, we refer as "Sy2" for both the Sy1.9 and Sy2 sources in the sample). We observe that on average, the mass of the central BH in Sy2

galaxies appear to be larger when compared to Sy1s, while their accretion rate appears to be smaller. The study of the significance of these differences is outside the scope of our project. However, we have to compare the mean PSD of Sy1 and Sy2 sources with the same BH mass and accretion rate in order to test whether they are similar or not, because the power spectrum may depend on BH mass and/or accretion rate.

The dashed lines in the upper panel of Fig. 9 indicate a box where the mean BH mass and accretion rate of the Sy1 and Sy2 galaxies in that box are approximately equal. Indeed, $\overline{\log(M_{BH})} = 7.61 \pm 0.12$ and 7.8 ± 0.10, while $\overline{\log(\lambda_{Edd})} = -1.28 \pm 0.07$ and -1.46 ± 0.06, for the Sy1s and Sy2s withing this box, respectively. Errors indicate the error of the mean, therefore the difference between the Sy1 and Sy2 mean $\log(M_{BH})$ and $\log(\lambda_{Edd})$ is consistent with zero within $\sim 1.1\sigma$ and 2σ, respectively.

The lower panel in Fig. 9 shows the mean PSD of all the Sy1 and Sy2 AGNs within the box in the top panel. The PSD was computed as discussed in Section (2.6). We fitted the power spectra with the model defined by eq. (13). The dashed lines in this panel show the best-fit lines to the mean PSDs, which provide a good description of the overall PSDs. The best fit line parameters are: $\log(PSD_{amp,\text{Sy1}}) = 0.20 \pm 0.21$, $\log(PSD_{amp,\text{Sy2}}) = 0.28 \pm 0.28$, and $PSD_{slope,\text{Sy1}} = -0.75 \pm 0.09$, $PSD_{slope,\text{Sy2}} = -0.81 \pm 0.13$. Clearly, the Sy1 and Sy2 PSDs are consistent, within the errors. This result suggests that the variability properties of the Sy1 and Sy2 galaxies in the $14 - 195\ keV$ band are identical. Thus, for the rest of our work, we combine together light-curves from Sy1 and Sy2 sources in order to investigate the dependence of the power spectrum on BH mass and/or accretion rate.

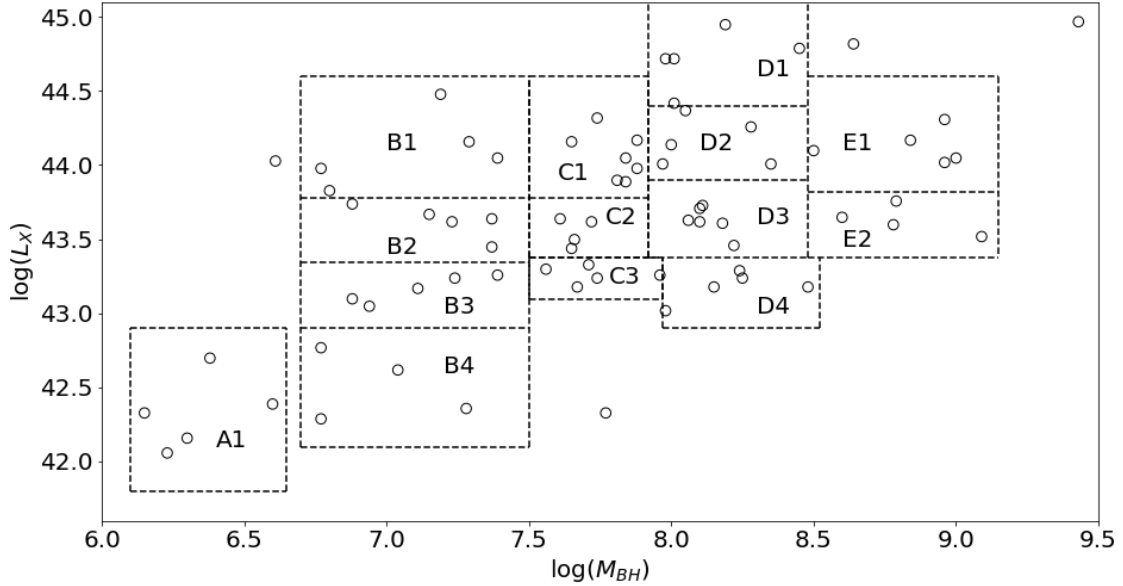## 3.3 Power spectrum dependence on Black Hole mass and X-ray luminosity

Figure 10: Diagram of $log(L_X)$ vs $log(M_{BH})$ for the variable sources in the sample. Dashed lines indicate the group of AGN that were used for our analysis.

Figure 10 shows a plot of the logarithm of X-ray luminosity, $log(L_X)$, vs the logarithm of BH masses, $log(M_{BH})$, for the variable AGN in the sample. We computed the X-ray luminosity, L_X, using the relation: $L_X = L_{Bol} - log(8)$, where L_{Bol} is the Bolometric luminosity (taken from Table 9, in Koss et al. (2022)). The dashed boxes in this figure indicate groups of AGN which have similar BH mass and L_X. Mean BH mass and L_X for the AGN in each group are listed in columns 2 and 3 of Table 1.

We computed the mean PSD of all AGN in each box as explained in section (2.6). We then fitted the mean PSD with the linear model defined by eq. (13). In order to investigate whether aliasing may affect the observed power-spectra, we first fitted them using the PSD estimates at frequencies lower than $10^{-1}(month^{-1})$, and then we fitted the full spectrum. The best-fit results are listed in the last two columns in Table 1 (values in parenthesis show the results in the case when we fit the full PSD). Figures 11-24 show a plot of the mean power-spectrum of the AGN in each group shown in Fig. 10. Black continuous and dotted lines indicate the best-fit lines when we fit the power spectrum below $10^{-1}(month^{-1})$ and when we consider all frequencies, respectively.

Table 1: Letters and numbers in the first column refer to the respective group, as labeled in Fig. 10. $log(PSD_{amp})$ and PSD_{slope} list the best fit amplitude and slope, respectively, when we fit the model line defined by eq. (13) to the power spectra at frequencies lower than $10^{-1}month^{-1}$. Values in parenthesis show the results when we fit the full PSDs. Columns $\overline{log(M_{BH})}$ and $\overline{log(L_X)}$ list the mean BH mass and mean X-ray luminosity of the AGN in each group, respectively.

| PSD Group	$\overline{log(M_{BH})}$	$\overline{log(L_X)}$	$log(PSD_{amp})$	PSD_{slope}
A1	6.33 ± 0.08	42.32 ± 0.11	0.05 ± 0.25	-1.17 ± 0.50
			(-0.03 ± 0.37)	(-0.92 ± 0.22)
B1	7.09 ± 0.13	44.10 ± 0.11	0.16 ± 0.27	-1.00 ± 0.31
			(0.06 ± 0.45)	(-0.69 ± 0.22)
B2	7.20 ± 0.09	43.62 ± 0.05	0.06 ± 0.18	-0.86 ± 0.26
			(-0.08 ± 0.18)	(-0.58 ± 0.15)
B3	7.11 ± 0.09	43.16 ± 0.04	0.27 ± 0.27	-1.03 ± 0.19
			(0.26 ± 0.30)	(-1.01 ± 0.14)
B4	6.96 ± 0.12	42.51 ± 0.11	0.64 ± 0.40	-1.14 ± 0.17
			(0.44 ± 0.34)	(-0.65 ± 0.08)
C1	7.81 ± 0.03	44.06 ± 0.06	0.48 ± 0.31	-1.17 ± 0.29
			(0.51 ± 0.37)	(-1.23 ± 0.22)
C2	7.66 ± 0.02	43.55 ± 0.05	0.27 ± 0.33	-1.06 ± 0.33
			(0.07 ± 0.20)	(-0.55 ± 0.11)
C3	7.73 ± 0.07	43.26 ± 0.03	0.40 ± 0.29	-0.99 ± 0.15
			(0.23 ± 0.24)	(-0.66 ± 0.10)
D1	8.13 ± 0.09	44.72 ± 0.09	0.01 ± 0.32	-1.10 ± 0.28
			(-0.24 ± 0.25)	(-0.48 ± 0.12)
D2	8.13 ± 0.08	44.15 ± 0.07	0.27 ± 0.27	-0.37 ± 0.30
			(0.32 ± 0.28)	(-0.50 ± 0.17)
D3	8.13 ± 0.02	43.62 ± 0.04	0.44 ± 0.46	-1.20 ± 0.31
			(0.36 ± 0.44)	(-0.94 ± 0.19)
D4	8.22 ± 0.08	43.18 ± 0.05	0.86 ± 0.57	-1.10 ± 0.21
			(0.83 ± 0.72)	(-1.11 ± 0.20)
E1	8.85 ± 0.09	44.13 ± 0.05	0.87 ± 0.70	-1.46 ± 0.27
			(0.66 ± 0.48)	(-1.00 ± 0.13)
E2	8.81 ± 0.10	43.63 ± 0.05	0.13 ± 0.15	-0.43 ± 0.23
			(0.36 ± 0.37)	(-1.06 ± 0.20)
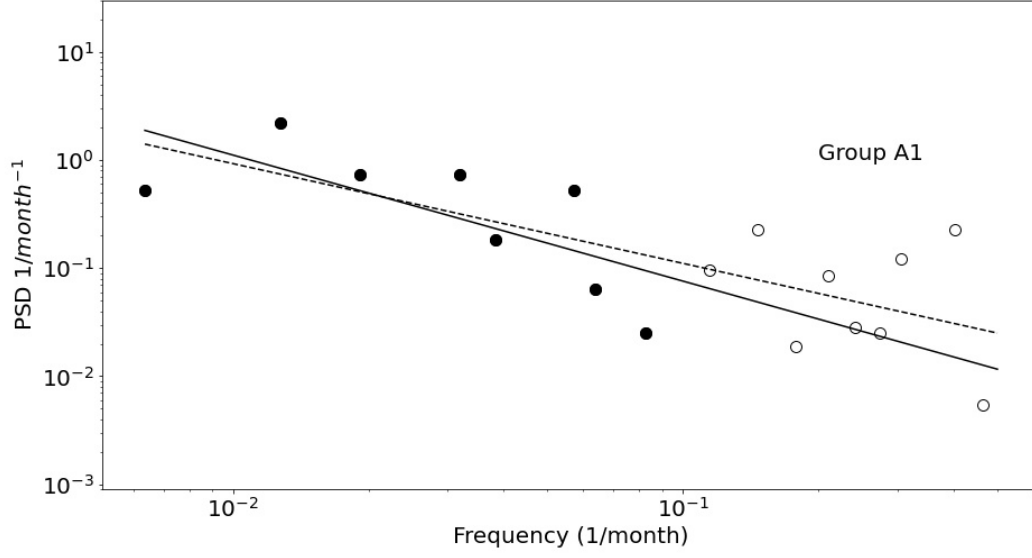
Figure 11: Mean power spectrum of the AGN in group A1. Black filled and open circles show the power spectrum estimates at frequencies below and above $10^{-1}(month^{-1})$. Black continuous and dashed line shows the best-fit lines when we fit the power spectrum below $10^{-1}(month^{-1})$ and when we consider all frequencies, respectively.
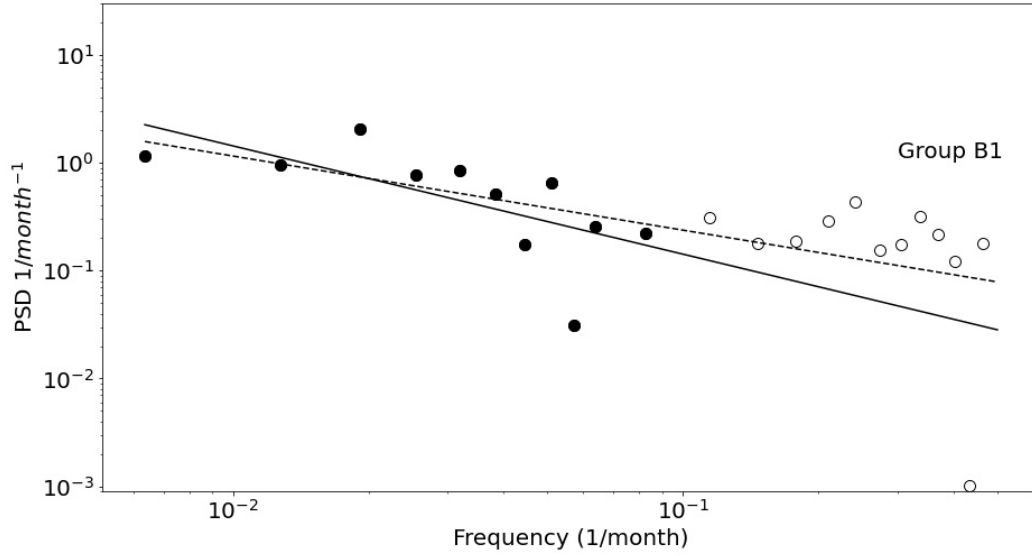

Figure 12: Same as in Fig. 11 , but for AGN in group B1.
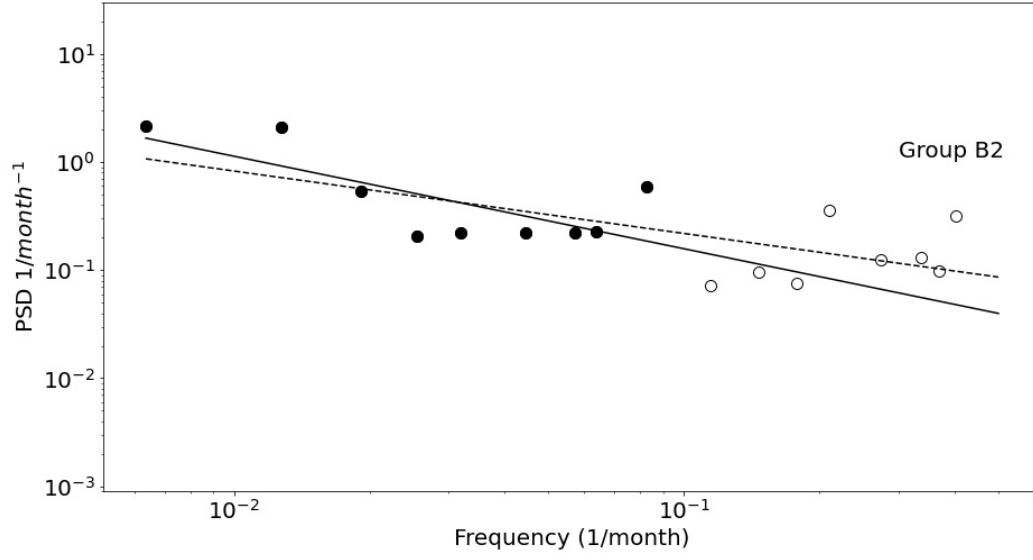
Figure 13: Same as in Fig. 11 , but for AGN in group B2.

Figure 14: Same as in Fig. 11 , but for AGN in group B3.

Figure 15: Same as in Fig. 11 , but for AGN in group B4.

Figure 16: Same as in Fig. 11 , but for AGN in group C1.

Figure 17: Same as in Fig. 11 , but for AGN in group C2.

Figure 18: Same as in Fig. 11 , but for AGN in group C3.

Figure 19: Same as in Fig. 11 , but for AGN in group D1.

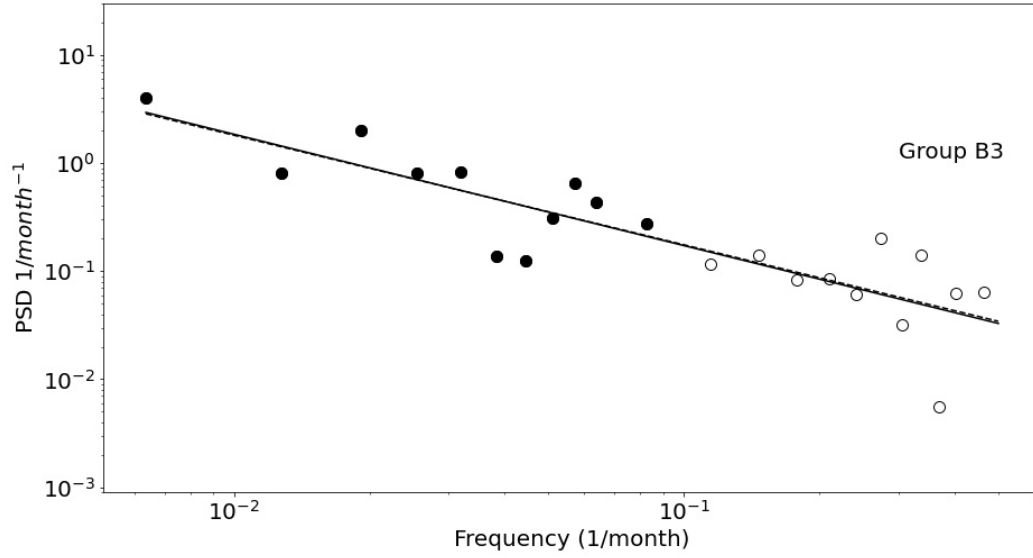**Figure 20:** Same as in Fig. 11 , but for AGN in group D2.

Figure 21: Same as in Fig. 11 , but for AGN in group D3.

Figure 22: Same as in Fig. 11 , but for AGN in group D4.

Figure 23: Same as in Fig. 11 , but for AGN in group E1.

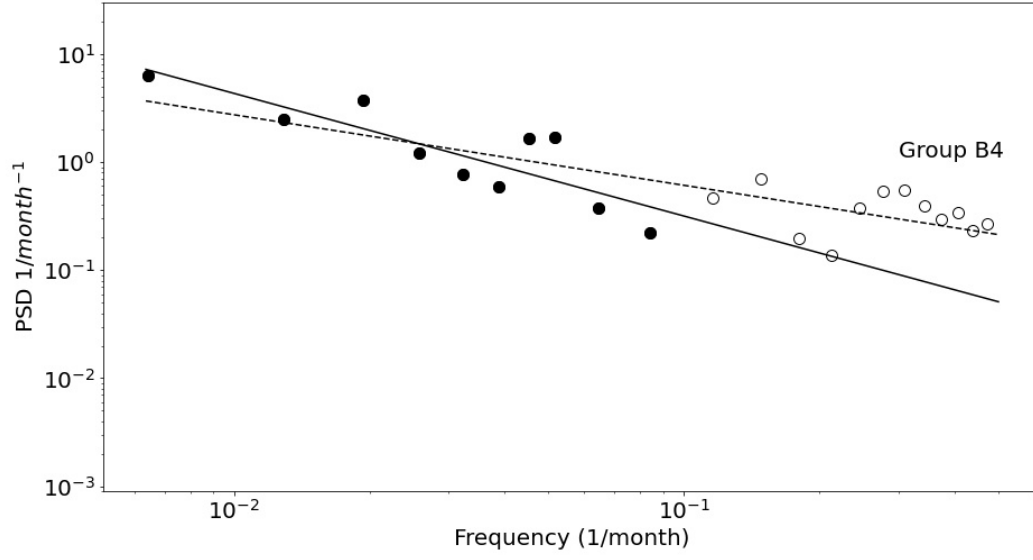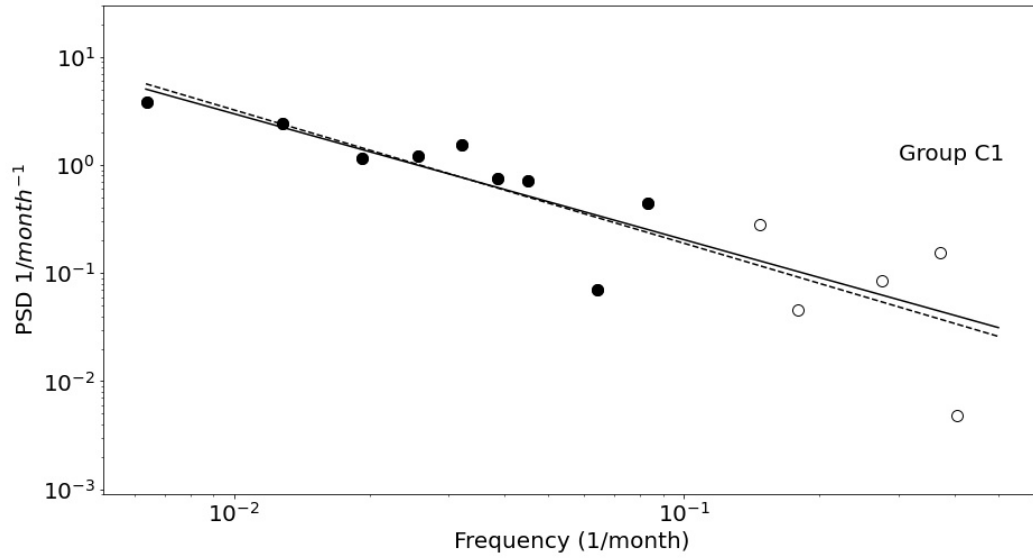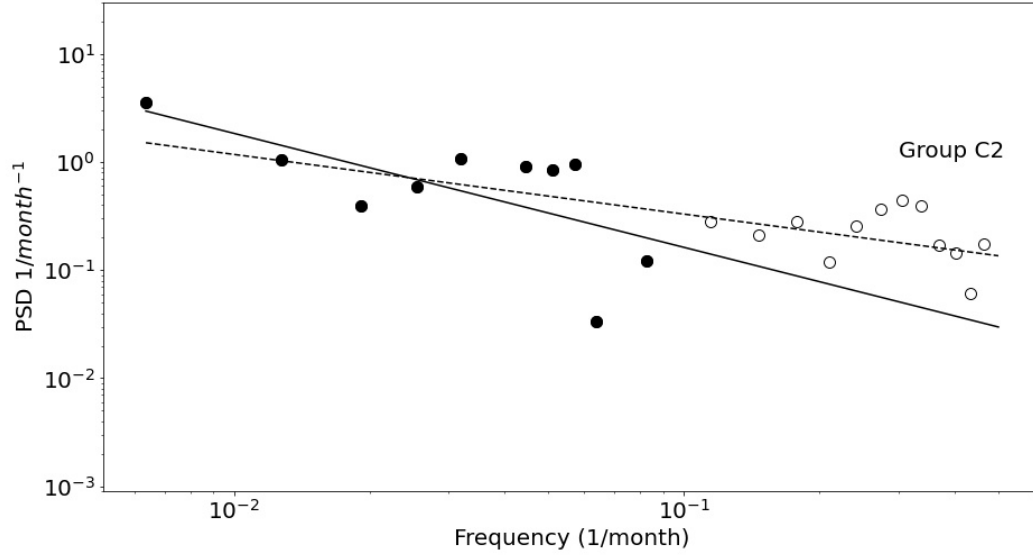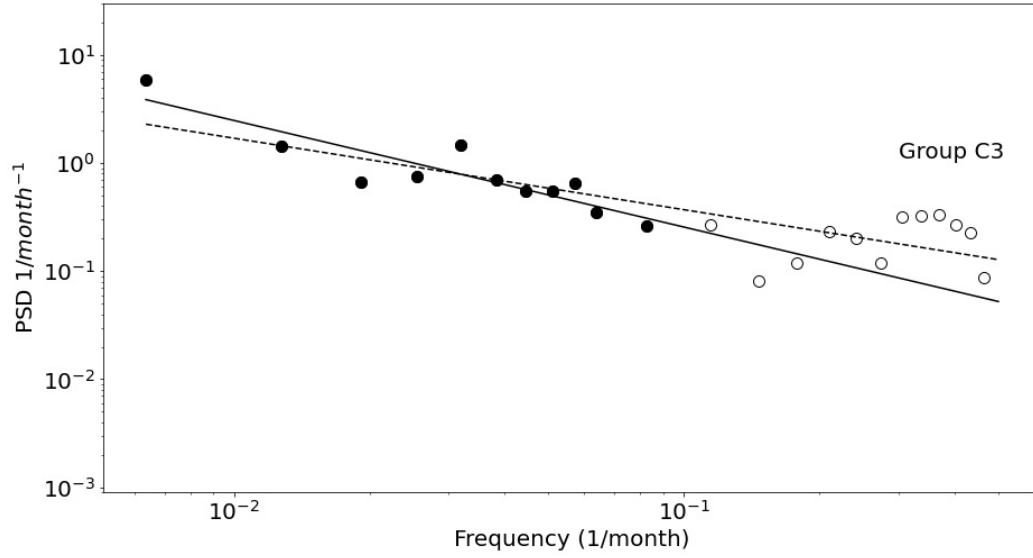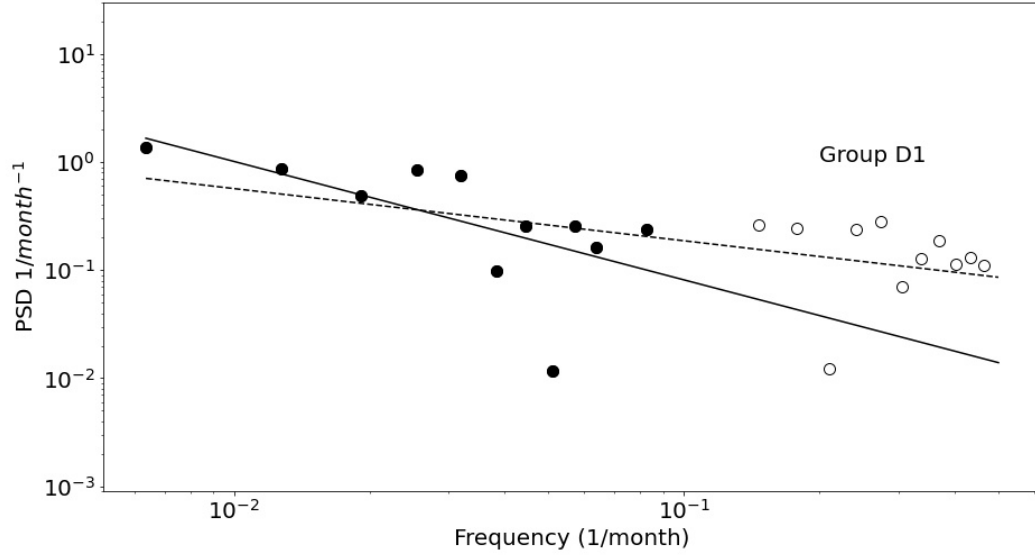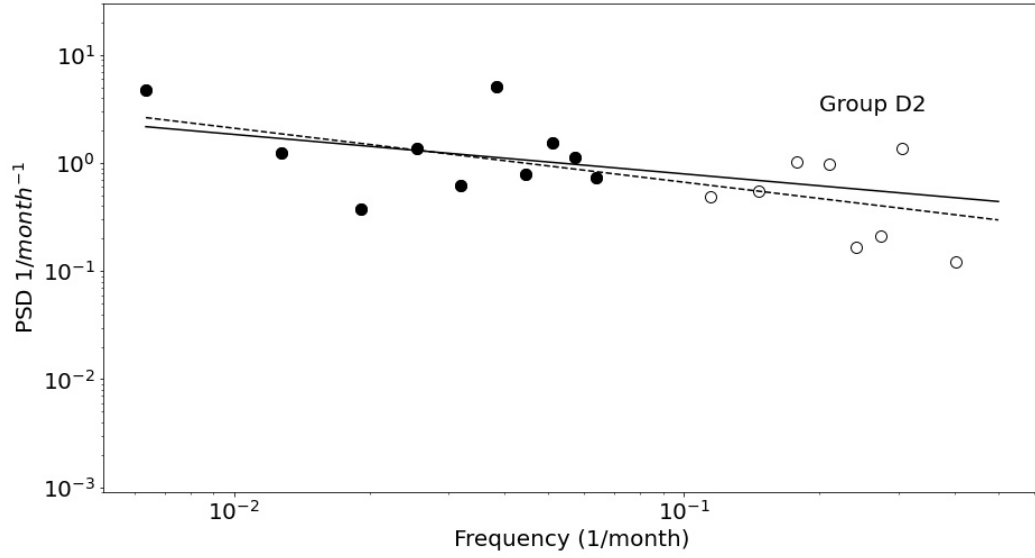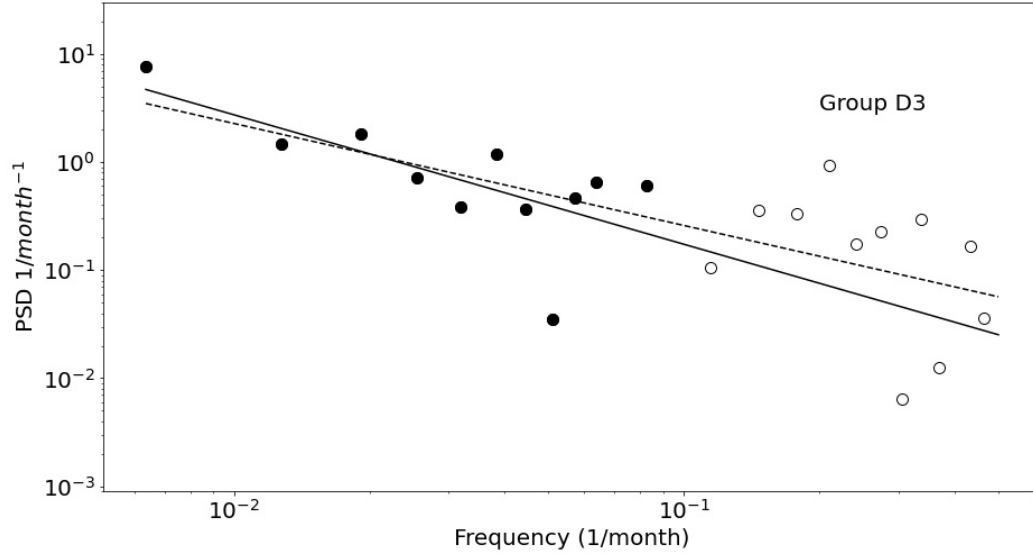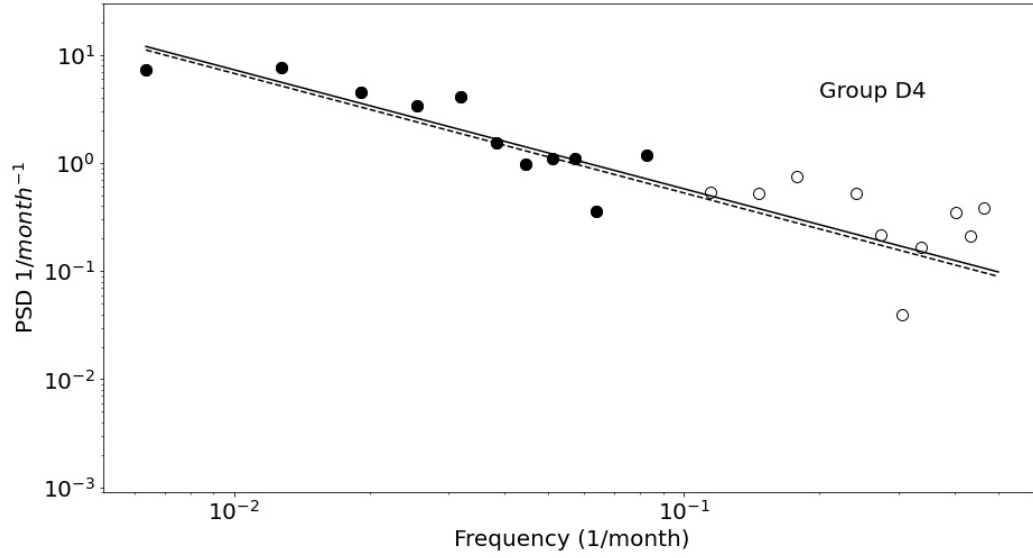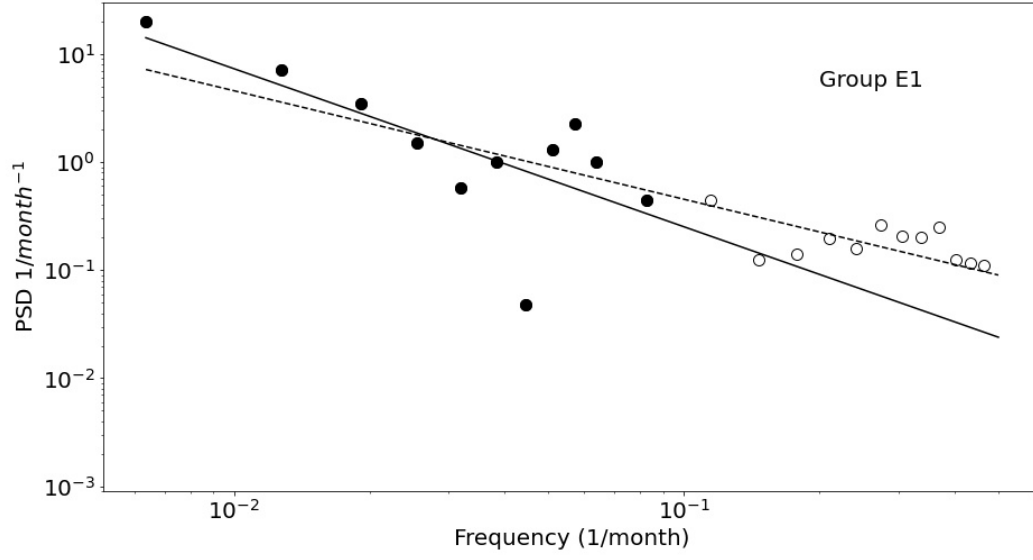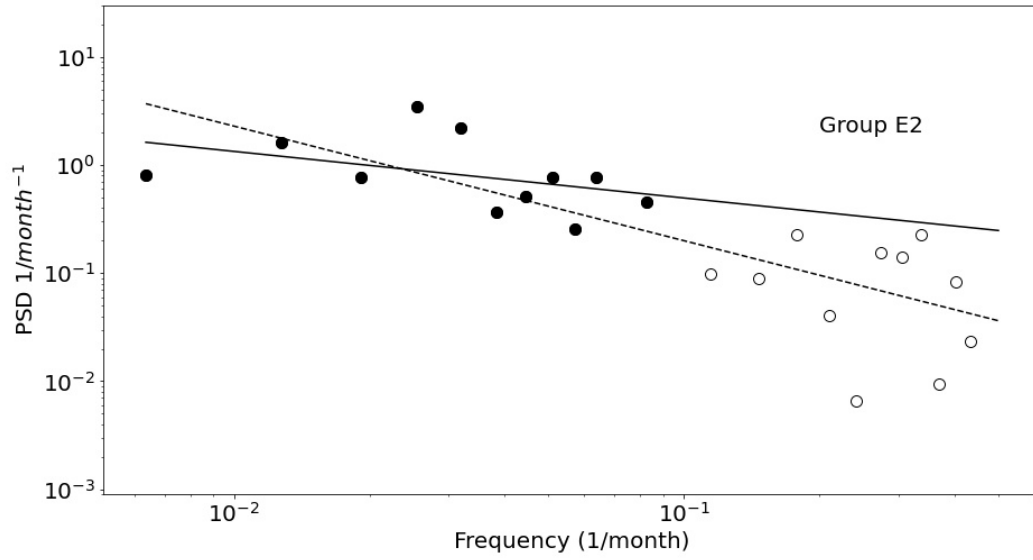**Figure 24:** Same as in Fig. 11 , but for AGN in group E2.

Figures 25 and 26 show the best-fit PSD_{slope} and $log(PSD_{amp})$ versus the mean BH mass of AGN in each bin, $\overline{log(M_{BH})}$, respectively. Filled circles show the best fit results when we fit the low-frequency PSD, while open circles show the values when we fit the full PSD. We computed the weighted mean of PSD_{slope} and $log(PSD_{amp})$ in each case. The results are as follows: $\overline{PSD_{slope,lf}} = -1.00 \pm 0.06$, $\overline{PSD_{slope,full}} = -0.74 \pm 0.04$, $\overline{log(PSD_{amp,lf})} = 0.21 \pm 0.07$ and $\overline{log(PSD_{amp,full})} = 0.14 \pm 0.08$[3]. Red solid/dashed lines in Figs. 25 and 26 show the weighted mean in the case when we fit the low frequencies/full PSDs, respectively.

The $log(PSD_{amp})$ weighted means are consistent with each other, within the errors. However, this is not the case for the best-fit PSD slopes. The weighted mean of the PSD best-fit slopes when we fit the PSD at low frequencies only is significantly steeper than $\overline{PSD_{slope,full}}$ (at the $\sim 3.6\sigma$ level). These results could be due to the aliasing effect (see figure 8). We therefore accept the results from the fits to the low frequency PSDs as more representative of the intrinsic X-ray PSD of AGN.

We test whether the PSD slope and amplitude is the same in all AGN by fitting a constant line ($y = \overline{PSD_{slope,lf}}$ and $y = \overline{log(PSD_{amp,lf})}$) to the data plotted in Figs. 25 and 26. The best fit χ^2 is 15.8/13dof and 6.8/13dof, which implies that both the PSD slope and amplitude is the same for all AGN.

---

[3]The weighted mean was calculated using the equation we mentioned in footnote 2, while its errors where calculated as $\sigma_w = 1/\sqrt{\sum \frac{1}{\sigma_i^2}}$, where σ_i is the error of x_i.

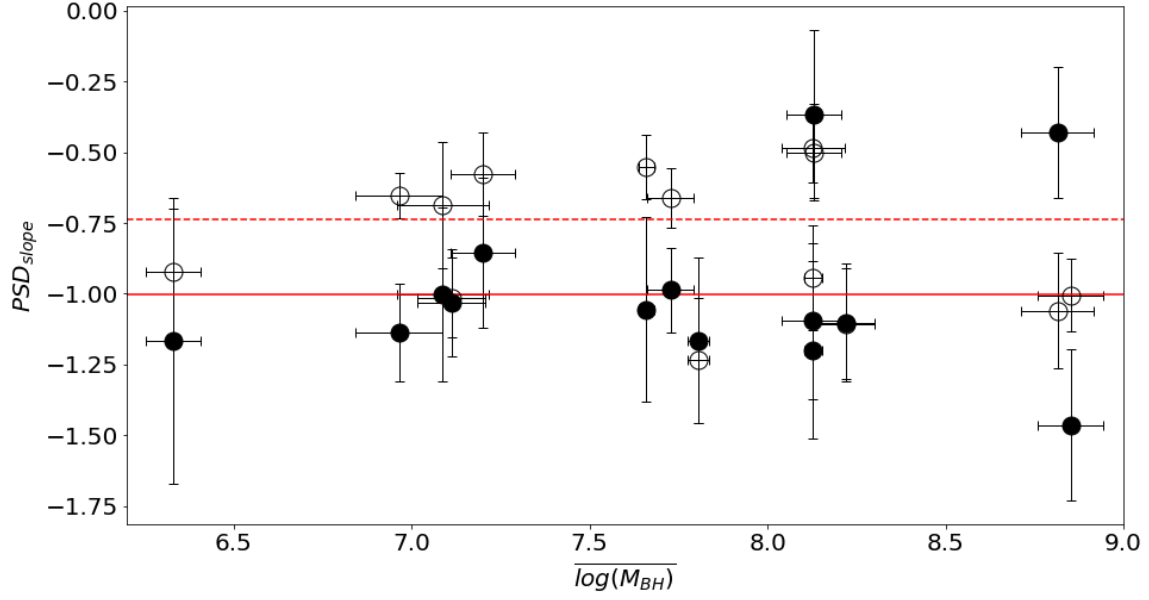**Figure 25:** PSD_{slope} vs $\overline{\log(M_{BH})}$. Filled and open circles show the best-fit PSD_{slope} values versus the mean BH mass in each bin, when we fit the low-frequency and the full PSD, respectively.
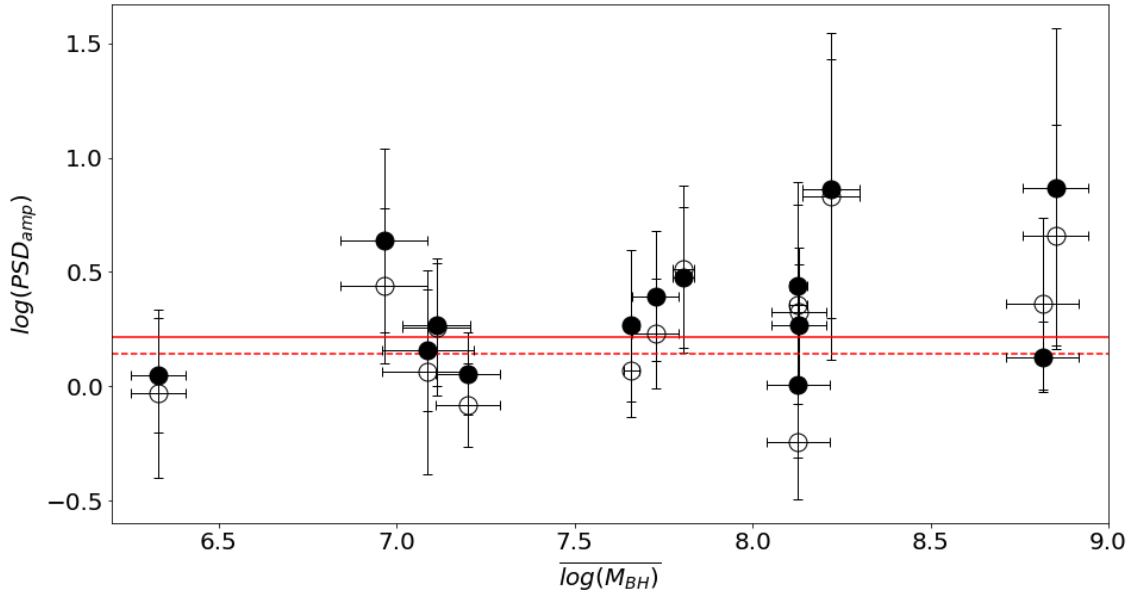

Figure 26: Same as in figure 25
for the best fit $log(PSD_{amp})$.

CHAPTER 4: SUMMARY AND CONCLUSIONS

4.1 Summary

The main objective of this work was to study the long term variability of AGN in hard X-rays. To this end, we considered the 100 brightest (highest flux) AGN in the $14 - 15\,keV$ band of the Koss et al. (2022) sample. This sample consists of AGN that have been detected by BAT on board *Swift* satellite. There are 858 AGN in this sample. This sample represents a census of the brightest hard X-ray selected AGN in the sky, spanning many orders of magnitude in black hole mass ($M_{BH} = 10^5 - 10^{10} M_{\odot}$), and AGN bolometric luminosity ($L_{bol} = 10^{40} - 10^{47} ergs^{-1}$). The sub-sample we considered also spans a large range of BH masses and bolometric luminosity (see Fig. 10). This group of objects is ideal for variability studies as each one of them has been observed continuously by *Swift* BAT for 157 months, i.e. more than 13 years.

First, we used the BAT light curves in order to find out which one of the AGN is variable or not. We fitted the light curves with a constant line, equal to the light curve weighted mean, and we found that 26 AGN are non-variable, i.e. the light curve is consistent with being constant during the BAT observations.

We calculated the power spectrum for every AGN in our sample and we subtracted the poisson noise level from them. In order to check the validity of our poisson noise estimation prescription we compared the predicted poisson noise level with the observed power spectra of the non-variable AGN. We found that they are consistent with each other, which implies that the poisson noise level estimation formula should be correct.

We grouped AGN in bins with a width of $\Delta log(M_{BH}) \sim 0.4$ and $\Delta log(L_X) \sim 0.4$. There are approximately 4 to 5 sources in each bin. We computed the mean PSD of all AGN in each group as explained in Section (2.6). The power spectra are plotted in Figs. 11-24. We fitted them with a straight line (in the log-log space) as defined by eq. (13). We fitted the power spectra both at frequencies below $10^{-1}(month^{-1})$ and at all frequencies, because we wanted to investigate if aliasing affects the observed power spectra. We found that the low frequency amplitude remains the same, while the slope flattens when we fit the full power spectrum. This could be the effect of aliasing. We therefore consider the results from the fits at low frequencies.

4.2 Main results

This work represents the most comprehensive analysis of the X-ray variability of AGN at energies above $15\,keV$. Our main results can be summarized as follows:

- We consider Type 1 and Type 2 AGN with the same BH mass and accretion rate. Their mean power spectrum is almost identical. Therefore variability properties must be identical for both Type 1 and Type 2 AGN. Photons with energies above $10\,keV$ should not be absorbed by the obscuring taurus. This implies that BAT data sample emission from the central source in both type of objects. The fact that the variability properties are the same for type 1 and 2 AGN suggests that the central source in these objects must operate in the same way. This is fully consistent with the unification theory of AGN.

- A power-law model of the form, $P(f) \propto f^{-a}$, fits well the PSDs of all objects. We do not detect any periodicity, or a frequency break to a different slope over the frequency range we probe with the BAT light curves ($\frac{1}{13years} - \frac{1}{2months}$).

- We found that the power spectrum has a slope of -1, same in all objects irrespective of BH mass and/or accretion rate. This is consistent with X-ray variability studies of a few AGN on long time scales in the $2 - 10\,keV$ band (Markowitz et al. (2003)).

- We found that the power spectrum amplitude at $f_0 = 10^{-2}(month^{-1})$ is $1.61/(month^{-1})$, irrespective of BH mass and/or accretion rate. Assuming that the power spectrum slope is -1, this implies that

28

the power spectrum amplitude in terms of $f \cdot PSD(f)$ is equal to $(1.6 \pm 0.3) \cdot 10^{-2}$ at all frequencies up to the break frequency, where the power spectrum slope will steepen to -2. This value is larger than the respective median value of $3 \cdot 10^{-3}$ that has been measured in a few nearby AGN in the $2 - 10\ keV$ band (Gonzalez Martin & Vaughan (2011)). Interestingly, our value is fully consistent with the power spectrum amplitude of Cyg X-1 in the soft state in the $6 - 13\ keV$ band (Churazov E., Gilfanov M. & Revnivtsev M. (2001); Reig P., Papadakis I. & Kylafis N. D. (2003)).

APPENDIX A

Table 2: AGN in the sample and their properties.

Source	DR2 Type[a]	$F^{obs}_{14-195\text{keV}}$[b]	z[a]	$\log(\text{M}_{\text{BH}})$[a]	$\log(\lambda_{\text{Edd}})$[a]	χ^2/dof[c]	V/NV[d]
CenA	Sy2	1346.34	0.0019	7.77	-2.72	80640.65/156	V
NGC4151	Sy1	618.88	0.0032	7.56	-1.53	25562.30/156	V
NGC2110	Sy2	328.93	0.0075	8.78	-2.46	7188.11/156	V
NGC4945	Sy2	282.11	0.0023	6.15	-1.09	2129.02/156	V
NGC4388	Sy2	278.91	0.0083	6.94	-1.17	5008.13/155	V
CircinusGalaxy	Sy2	273.17	0.0015	6.23	-1.44	525.07/156	V
IC4329A	Sy1	263.25	0.0160	7.65	-0.77	1371.12/156	V
NGC5506	Sy1.9	239.40	0.0060	7.24	-1.28	597.65/153	V
4C+50.55	Sy1.9	210.38	0.0154	7.97	-1.24	1405.12/156	V
MCG-5-23-16	Sy1.9	209.62	0.0084	7.65	-1.49	827.79/156	V
NGC4507	Sy2	184.54	0.0117	7.81	-1.18	993.72/156	V
NGC3783	Sy1	173.84	0.0090	7.37	-1.2	736.34/156	V
NGC7172	Sy2	160.02	0.0085	8.15	-2.25	875.63/152	V
Mrk3	Sy1.9	150.12	0.0138	8.96	-2.21	1343.69/156	V
CygnusA	Sy2	145.23	0.0565	9.43	-1.74	947.41/156	V
Mrk348	Sy1.9	144.81	0.0147	6.8	-0.25	1357.28/156	V
UGC3374	Sy1	141.21	0.0202	6.61	0.15	1260.05/153	V
IRAS05078+1626	Sy1	119.80	0.0174	6.88	-0.41	994.33/151	V
1RXSJ173728.0-290759	Sy1.9	119.04	0.0218	7.84	-1.07	719.70/145	V
3C111	Sy1	118.67	0.0497	8.45	-0.94	692.25/152	V
NGC3227	Sy1	112.47	0.0033	6.77	-1.28	648.91/153	V
NGC3516	Sy1	112.42	0.0087	7.39	-1.41	1561.91/156	V
4U1344-60	Sy1.9	111.79	0.0128	9.09	-2.85	211.47/156	V
Mrk926	Sy1	110.22	0.0477	7.98	-0.54	605.22/155	V
ESO103-35	Sy1.9	106.86	0.0135	7.37	-1.01	553.05/156	V
NGC5252	Sy2	103.15	0.0230	9.0	-2.23	1352.73/155	V
3C390.3	Sy1	102.87	0.0556	8.64	-1.1	772.56/156	V
Mrk509	Sy1	100.14	0.0347	8.05	-0.96	526.51/153	V
MR2251-178	Sy1	99.53	0.0645	8.19	-0.52	370.15/153	V
NGC6300	Sy2	96.37	0.0031	6.77	-1.75	701.76/156	V
3C120	Sy1	95.38	0.0331	7.74	-0.7	697.27/155	V
ESO506-27	Sy2	90.68	0.0242	8.84	-1.94	1038.69/154	V
NGC4593	Sy1	88.30	0.0083	6.88	-1.05	233.36/153	V
NGC5548	Sy1	86.47	0.0167	7.72	-1.37	1129.77/156	V
NGC5728	Sy1.9	84.74	0.0103	8.25	-2.28	611.12/154	V
NGC1275	Sy1.9	82.64	0.0168	8.6	-2.23	649.27/156	V
3C382	Sy1	82.33	0.0579	8.01	-0.56	473.91/156	V
NGC7582	Sy2	82.28	0.0052	7.74	-1.78	523.49/155	V
NGC3081	Sy2	81.89	0.0081	7.67	-1.76	526.76/156	V
NGC3281	Sy2	81.21	0.0111	8.22	-2.04	479.64/156	V
NGC788	Sy2	77.51	0.0137	8.18	-1.84	585.38/156	V
NGC1142	Sy2	74.31	0.0287	8.96	-1.93	730.35/156	V

Ark120	Sy1	74.29	0.0326	8.07	-1.18	176.15/156	NV
NGC526A	Sy1.9	73.91	0.0189	8.06	-1.71	699.07/156	V
NGC7469	Sy1	70.63	0.0160	6.96	-0.72	182.87/155	NV
IC5063	Sy2	67.76	0.0113	8.24	-2.22	545.68/156	V
ESO297-18	Sy2	67.37	0.0252	8.5	-1.67	219.67/156	V
NGC6814	Sy1	64.47	0.0058	7.04	-1.7	777.90/150	V
NGC1365	Sy1	63.52	0.0051	6.6	-1.49	322.18/156	V
NGC1365	Sy1	63.52	0.0051	6.6	-1.49	322.18/156	V
IRAS05589+2828	Sy1	62.28	0.0331	8.0	-1.13	836.57/147	V
Mrk1040	Sy1	62.22	0.0163	7.41	-1.18	193.46/154	NV
Mrk110	Sy1	60.95	0.0352	7.29	-0.41	214.51/156	V
MCG-6-30-15	Sy1	59.53	0.0071	6.6	-1.1	174.65/155	NV
ESO141-55	Sy1	58.77	0.0371	7.99	-1.09	174.08/156	NV
LEDA178130	Sy2	58.27	0.0352	7.88	-0.99	311.22/156	V
NGC7314	Sy1.9	57.42	0.0046	6.3	-1.42	211.06/153	V
Mrk1210	Sy1.9	57.40	0.0136	6.86	-0.79	198.27/155	NV
Mrk6	Sy1	56.70	0.0190	8.1	-1.76	586.66/156	V
LEDA138501	Sy1	55.63	0.0497	8.01	-0.86	234.89/156	V
NGC4992	Sy2	54.42	0.0252	8.59	-1.93	195.39/155	NV
LEDA168563	Sy1	54.10	0.0283	7.88	-1.18	273.67/156	V
NGC7603	Sy1	52.96	0.0287	8.59	-1.95	129.26/150	NV
NGC235A	Sy1.9	52.14	0.0221	8.49	-2.06	180.41/156	NV
NGC6860	Sy1.9	51.52	0.0147	7.71	-1.65	338.31/156	V
4C+74.26	Sy1	51.18	0.1050	9.83	-2.0	183.93/156	NV
2MASSJ07594181-3843560	Sy1	51.15	0.0400	8.82	-1.89	180.72/156	NV
LEDA38038	Sy2	49.46	0.0277	8.11	-1.53	184.09/156	NV
LEDA86269	Sy2	49.38	0.0105	7.98	-2.24	484.86/152	V
NGC612	Sy2	48.97	0.0299	8.28	-1.3	322.18/156	V
ESO362-18	Sy1	48.89	0.0125	7.11	-1.22	216.20/156	V
NGC973	Sy2	48.41	0.0157	8.48	-2.58	1045.03/156	V
Fairall9	Sy1	48.39	0.0459	8.3	-1.23	172.59/156	NV
HE1143-1810	Sy1	48.28	0.0326	7.39	-0.62	215.05/156	V
MCG-1-24-12	Sy2	46.38	0.0196	7.66	-1.44	213.07/156	V
LEDA166252	Sy1	44.90	0.0249	8.79	-2.31	302.68/156	V
1RXSJ165605.6-520345	Sy1	43.23	0.0538	8.33	-1.16	177.28/156	NV
Mrk1498	Sy1	42.97	0.0558	7.19	0.02	493.22/156	V
Mrk79	Sy1	42.72	0.0221	7.61	-1.25	457.84/156	V
NGC4051	Sy1	42.49	0.0020	6.13	-1.72	169.25/156	NV
2MASXiJ1802473-145454	Sy1	42.36	0.0343	7.98	-1.28	157.24/152	NV
1RXSJ174155.3-121157	Sy1	41.54	0.0376	8.03	-1.18	168.96/154	NV
ESO548-81	Sy1	41.21	0.0144	7.96	-1.97	337.36/156	V
3C445	Sy1	39.82	0.0561	7.89	-0.6	150.83/153	NV
ESO490-26	Sy1	39.49	0.0252	7.15	-0.76	224.91/155	V
IGRJ21277+5656	Sy1	39.43	0.0149	7.15	-1.22	172.84/156	NV
ESO511-30	Sy1	39.27	0.0229	7.23	-0.88	202.05/155	V
Fairall272	Sy2	39.15	0.0222	8.11	-1.66	223.64/155	V
IC4709	Sy2	39.08	0.0169	7.81	-1.69	171.50/156	NV
NGC7213	Sy1	39.04	0.0048	7.13	-2.08	164.71/155	NV
NGC4235	Sy1	38.62	0.0079	7.28	-2.2	443.00/153	V
NGC1068	Sy1.9	37.90	0.0035	6.93	-1.56	182.20/156	NV

PictorA	Sy1	37.32	0.0350	6.77	-0.07	264.56/156	V
Mrk704	Sy1	36.84	0.0295	8.24	-1.76	169.00/151	NV
NGC3079	Sy2	36.74	0.0035	6.38	-0.95	203.91/156	V
Fairall51	Sy1	36.51	0.0139	7.11	-1.21	181.93/156	NV
NGC7319	Sy2	36.45	0.0226	8.1	-1.67	209.13/156	V
NGC1194	Sy2	36.22	0.0136	7.83	-1.49	154.44/156	NV
CTS109	Sy1	35.80	0.0300	7.84	-1.23	228.57/153	V
Z121-75	Sy1	35.66	0.0331	7.27	-0.61	177.16/152	NV
LEDA170194	Sy2	35.33	0.0363	8.35	-1.62	221.19/153	V

Notes: [a] Taken from Koss et al. (2022). [b] Taken from the *Swift*-BAT 157 month survey (in units of 10^{-12} ergs/s/cm^2). [c] The χ^2, and the number of degrees of freedom (dof) when we fit a constant line to the light curves. [d] Classification of the variable (V) and non-variable (NV) sources, depending on p_{null} (see text for details).

REFERENCES

Churazov E., Gilfanov M. & Revnivtsev M., 2001, MNRAS, 321, 759.

Edelson R., Gelbord J., Cackett E. et al., 2019, ApJ, 870, 17.

Isobe T., Feigelson E. D., Akritas M. G. et al., 1990, ApJ, 364, 104.

Koss M. J., Ricci C., Trakhtenbrot B. et al, 2022, ApJS, 261, 30.

Krawczyk C. M., Richards G. T., Mehta S. S. et al, 2013, ApJS, 206, 19.

Markowitz A., Edelson R., Vaughan S. et al, 2003, ApJ, 593, 96.

Oh K., Koss M., Markwardt C. B. et al., 2018, ApJS, 235, 4.

Papadakis I. E. & Lawrence A., 1993, MNRAS, 261, 612.

Peterson B. M., An Introduction to Active Galactic Nuclei, 1997.

Priestley M. B., Spectral Analysis and Time Series volume 1, 1981.

Reig P., Papadakis I. & Kylafis N. D., 2003, A&A, 398, 1103.